Cell Reports
Medicine

Article

LTA4H improves the tumor microenvironment and prevents HCC progression via targeting the HNRNPA1/LTBP1/TGF-β axis

Graphical abstract

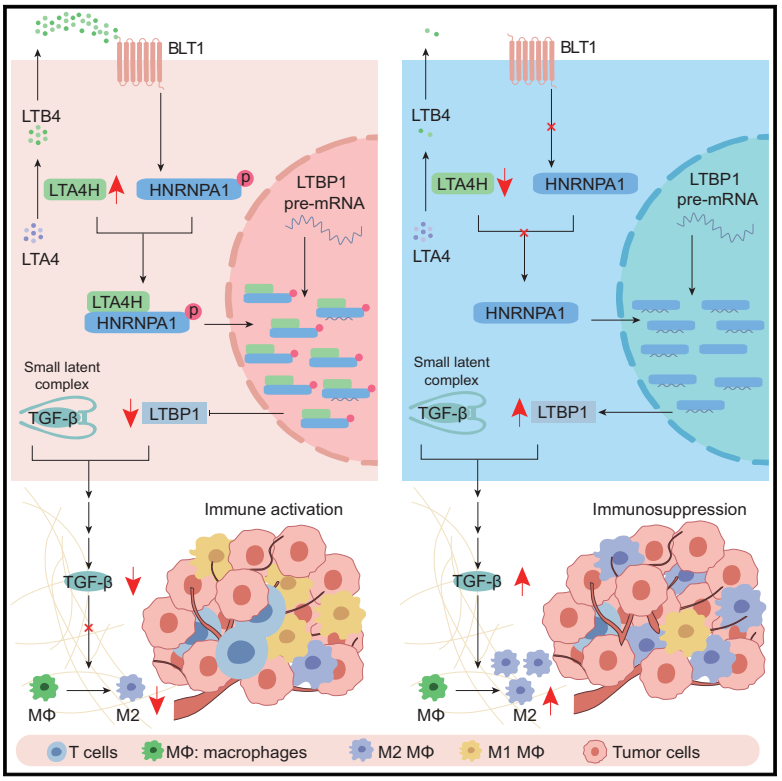

Highlights

- Downregulated LTA4H promotes HCC occurrence and progression
- LTA4H ablation fosters CD206^{+} macrophage via LTBP1-mediated TGF-β activation
- LTA4H prevents LTBP1 mRNA maturation and processing in an HNRNPA1-dependent manner
- TGF-β blockage sensitizes LTA4H-deficient HCC to immunotherapy

Authors

Shuai Yang (杨帅), Xinyao Qiu (邱辛瑶), Yingcheng Yang (杨应成), ..., Siyun Shen (莘似韵), Hongyang Wang (王红阳), Lei Chen (陈磊)

Correspondence

hywangk@vip.sina.com (H.W.), chenlei@smmu.edu.cn (L.C.)

In brief

Yang et al. report that LTA4H deficiency promotes CD206^{+} macrophage polarization through upregulating LTBP1 and downstream TGF-β secretion and activation in HCC. Mechanistically, LTA4H induces HNRNPA1 phosphorylation, enhancing their interaction and leading to functional inhibition of HNRNPA1 in regulating LTBP1 mRNA processing.

Yang et al., 2025, Cell Reports Medicine 6, 102000
March 18, 2025
https://doi.org/10.1016/j.xcrm.2025.102000

CellPress

Cell Reports Medicine

CellPress
OPEN ACCESS

Article

LTA4H improves the tumor microenvironment and prevents HCC progression via targeting the HNRNPA1/LTBP1/TGF-β axis

Shuai Yang (杨帅),[1,2,3,11] Xinyao Qiu (邱辛瑶),[1,2,3,11] Yingcheng Yang (杨应成),[4,11] Jing Wu (吴静),[3,5,11] Shan Wang (王珊),[2,3] Bo Zheng (郑博),[6] Jianmin Wu (吴建民),[7] Tao Zhou (周涛),[2,3] Yangqianwen Zhang (张杨倩雯),[2,3] Mixue Bai (白米雪),[2,3] Shuowu Liu (刘烁吾),[2,3] Zihan Zhao (赵紫涵),[2,3] Yani Zhang (张雅妮),[7] Yixian Wang (王溢贤),[7] Jinxia Bao (包金霞),[8] Mengye Wu (吴梦叶),[2,3] Dongdong Xue (薛冬冬),[2,3] Meiyu Bao (鲍美玉),[2,3] Ji Hu (胡继),[2,3] Siyun Shen (莘似韵),[2,3] Hongyang Wang (王红阳),[1,2,3,9,*] and Lei Chen (陈磊)[1,2,3,10,12,*]

[1]Fudan University Shanghai Cancer Center, Department of Oncology, Shanghai Medical College, Fudan University, Shanghai 200032, China
[2]The International Cooperation Laboratory on Signal Transduction, Eastern Hepatobiliary Surgery Hospital, Naval Medical University, Shanghai 200438, China
[3]National Center for Liver Cancer, Shanghai 200441, China
[4]Hepatic Surgery Department, Eastern Hepatobiliary Surgery Hospital, Naval Medical University, Shanghai 200438, China
[5]State Key Laboratory of Oncogenes and Related Genes, Shanghai Cancer Institute, Renji Hospital, Shanghai Jiao Tong University School of Medicine, Shanghai 200127, China
[6]Department of hematology, Naval medical center, Naval Medical University, Shanghai 200052, China
[7]Institute of Metabolism and Integrative Biology, Fudan University, Shanghai 200438, China
[8]Model Animal Research Center, Medical School, Nanjing University, Nanjing 210093, China
[9]Key Laboratory of Signaling Regulation and Targeting Therapy of Liver Cancer, Ministry of Education, Shanghai 200438, China
[10]Shanghai Key Laboratory of Hepatobiliary Tumor Biology (EHBH), Shanghai 200438, China
[11]These authors contributed equally
[12]Lead contact
*Correspondence: hywangk@vip.sina.com (H.W.), chenlei@smmu.edu.cn (L.C.)
https://doi.org/10.1016/j.xcrm.2025.102000

SUMMARY

Leukotriene A4 hydrolase (LTA4H), an inflammatory mediator, has garnered attention for its role in the development of chronic lung diseases and various cancers. Our study highlights the protective role of LTA4H in hepatocellular carcinoma (HCC) occurrence and progression. LTA4H is downregulated in clinical and mouse HCC tumors. LTA4H deficiency exacerbates hepatocyte damage by restraining JNK activation and promotes CD206$^+$ macrophage polarization through the upregulation of LTBP1 expression and downstream transforming growth factor β (TGF-β) secretion and activation. Mechanistically, LTA4H induces heterogeneous nuclear ribonucleoprotein A1 (HNRNPA1) phosphorylation, enhancing their interaction and leading to the functional inhibition of HNRNPA1 in regulating *Ltbp1* mRNA maturation and processing in the nucleus. LTA4H-deficient patients exhibit poor prognosis and immunotherapy resistance. Combination therapy targeting TGF-β and PD-1 significantly improves the immunotherapy resistance of LTA4H-knockout Hepa1-6 tumors. Our findings reveal the previously unreported role of LTA4H in regulating the tumor microenvironment and provide insights into potential diagnostic and therapeutic strategies for patients with LTA4H-deficient HCC.

INTRODUCTION

Hepatocellular carcinoma (HCC) is the most common primary liver cancer, ranking as the sixth most prevalent cancer and the third leading cause of cancer-related death globally.[1] Many patients are diagnosed at advanced stages, limiting curative treatment options and contributing to poor prognosis,[2] characterized by low 5-year survival rates and frequent recurrence after surgery. The inherent heterogeneity of HCC further complicates treatment strategies.[3] Chronic liver injury and inflammation, driven by factors such as viral hepatitis, alcohol-related liver disease, and nonalcoholic fatty liver disease, underlie HCC pathogenesis.[1] Inflammatory mediators critically influence the tumor microenvironment (TME) and drive HCC progression.

Understanding immune evasion mechanisms within the TME is key to improving immunotherapy outcomes in HCC. Tumor-associated macrophages (TAMs), which often adopt an M2-like phenotype, are abundant in HCC and serve as potential therapeutic targets.[4] Chemokines such as transforming growth factor β (TGF-β) and CCL2 are central to TAM recruitment and functional remodeling.[5,6] Reprogramming TAMs via chemokine signaling may synergize with immune checkpoint inhibitors (ICIs), though further research is needed to refine combinations and identify predictive biomarkers for patient stratification.

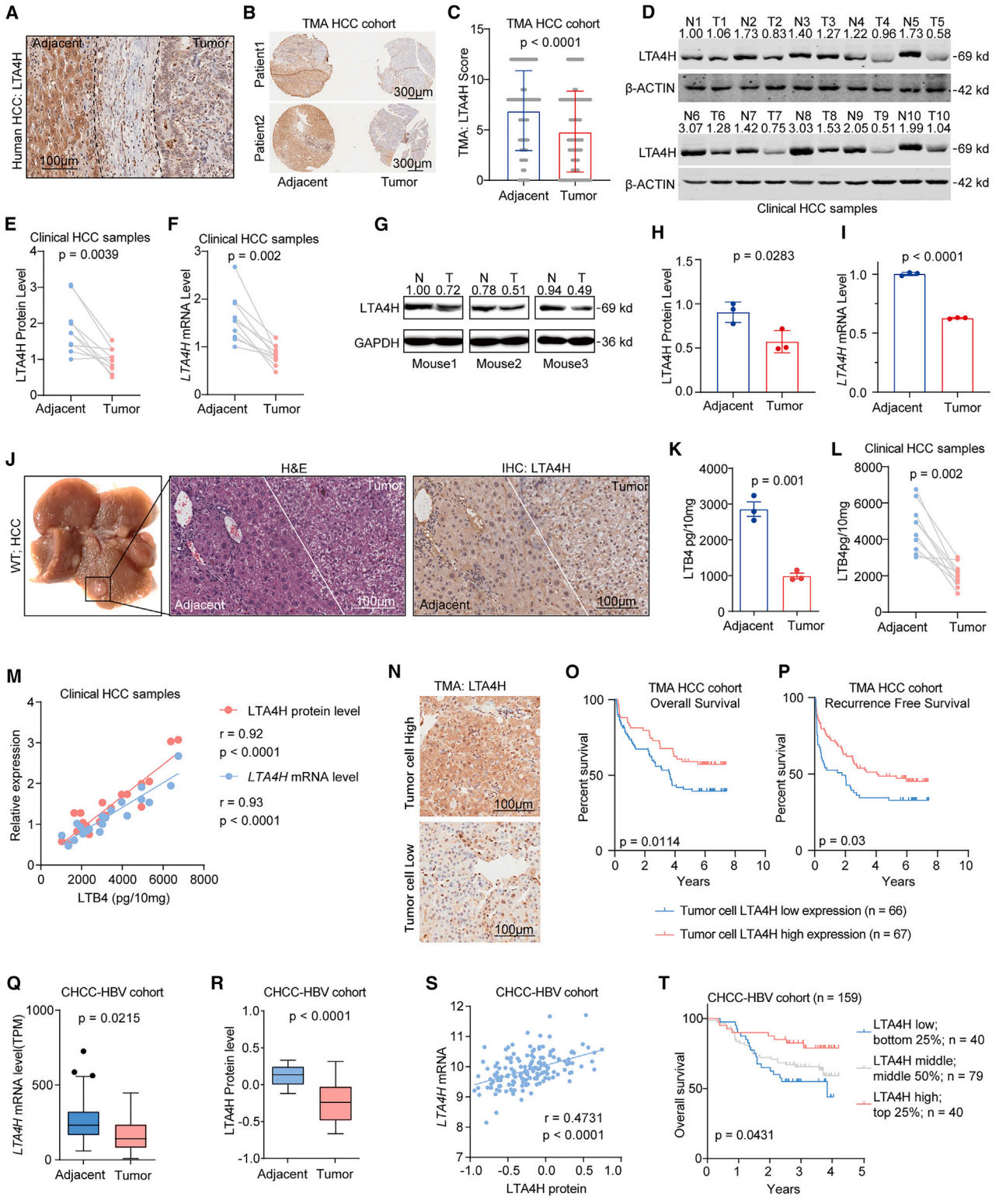

Figure 1. Downregulation of LTA4H was associated with poor prognosis in patients with HCC

(A) IHC detection of LTA4H in human HCC tissues.

(B and C) TMA analysis of LTA4H in HCC and para-tumor tissues.

(D and E) Western blot (WB) and quantification of LTA4H in clinical HCC samples.

(legend continued on next page)

Effective predictive biomarkers are essential to address the heterogeneous response of patients with HCC. Promising evidence suggests that RNA sequencing data can identify predictive signatures of therapeutic response from the TME.[7] However, translating these features into parameters measurable by immunohistochemistry (IHC) remains challenging but necessary for advancing clinical applications.

Leukotriene A4 hydrolase (LTA4H) is a multifunctional zinc metalloenzyme with epoxide hydrolase and aminopeptidase activities. It catalyzes the conversion of leukotriene A4 (LTA4) to leukotriene B4 (LTB4), a potent inflammatory mediator acting through leukotriene B4 receptor 1 (BLT1) and leukotriene B4 receptor 2 (BLT2) receptors.[8] LTA4H is highly expressed in several malignancies, including esophageal, skin, ovarian, and colorectal cancer,[9–11] where it promotes tumor progression by enhancing cell proliferation.[9–12] However, its role in liver cancer, particularly in modulating the TME, remains poorly understood.

In this study, we found that LTA4H deficiency promoted HCC occurrence and progression, correlating with poor prognosis. LTA4H-deficient models exhibited increased hepatocyte damage and M2-like macrophage infiltration as key drivers of HCC progression. Mechanistically, we showed that LTA4H regulates hepatocyte damage through c-Jun N-terminal kinases (JNK) activation and remodels the TME via the heterogeneous nuclear ribonucleoprotein A1 (HNRNPA1)-latent-transforming growth factor beta-binding protein 1 (LTBP1)-TGF-β signaling axis. We uncovered a previously undescribed role of nuclear LTA4H in mRNA processing and maturation, reprogramming macrophages to evade immune surveillance in HCC. Importantly, our findings support TGF-β blockade as an adjunct therapy to enhance ICI efficacy in patients with HCC with low LTA4H expression.

RESULTS

Downregulation of LTA4H was associated with poor prognosis in patients with HCC

To evaluate the clinical significance of LTA4H in HCC, we first analyzed the expression of LTA4H in human HCC tissue and paired adjacent tissues. IHC analysis of HCC sections and the tissue microarray (TMA) HCC cohort demonstrated that LTA4H expression was significantly downregulated in HCC (Figures 1A–1C). Similar to the IHC results, the protein and mRNA levels of LTA4H were lower in HCC tissues compared to matched adjacent tissues (Figures 1D–1F). We further examined the expression of LTA4H in a mouse HCC model induced by diethylnitrosamine (DEN). Consistent with our findings in clinical HCC samples, the transcript and protein levels of LTA4H were reduced in mouse HCC (Figures 1G–1J). LTB4, a key mediator of LTA4H function, was significantly downregulated in both mouse and human HCC (Figures 1K and 1L). Moreover, LTB4 levels showed a positive correlation with mRNA and protein level of LTA4H in clinical HCC samples (Figure 1M). We further assessed the relationship between LTA4H expression and survival. Patient characteristics are listed in Table S1. Both overall survival and recurrence-free survival were significantly shorter in patients with low LTA4H expression (Figures 1N–1P). Univariate and multivariate Cox regression analyses identified LTA4H expression as an independent risk factor for predicting overall survival and recurrence-free survival (Tables S1 and S2). To validate these findings, we performed the same analysis of HCC samples from the published Chinese HCC patients with HBV infection (CHCC-HBV) cohort.[13] Linear regression analysis revealed that LTA4H protein and transcript levels were decreased and positively correlated in the CHCC-HBV cohort (Figures 1Q–1S). Low LTA4H protein expression was also associated with poor prognosis in the CHCC-HBV cohort (Figure 1T). Together, these results indicated a repressive role for LTA4H in human HCC development.

Hepatocyte-specific LTA4H ablation promotes hepatocarcinogenesis

We constructed hepatocyte-specific LTA4H knockout ($LTA4H^{\Delta hep}$) and LTA4H knockout ($LTA4H^{KO}$) mice to study the role of LTA4H in a DEN-induced HCC model of $LTA4H^{f/f}$, $LTA4H^{\Delta hep}$, and $LTA4H^{KO}$ mice. $LTA4H^{\Delta hep}$ and $LTA4H^{KO}$ mice were generated by deleting the second exon of LTA4H (Figure S1A). 40 weeks after DEN injection, the absence of LTA4H expression correlated with increased liver-to-body weight ratios and tumor numbers in $LTA4H^{\Delta hep}$ and $LTA4H^{KO}$ mice. Unexpectedly, $LTA4H^{KO}$ mice developed significantly fewer tumors than $LTA4H^{\Delta hep}$ mice (Figures 2A–2D). Hepatocytic damage can be directly measured by alanine aminotransferase (ALT) and aspartate aminotransferase (AST) levels in the serum.[14] Compared with $LTA4H^{f/f}$ mice, $LTA4H^{\Delta hep}$ and $LTA4H^{KO}$ mice have higher plasma ALT and AST levels. However, no significant differences in plasma ALT or AST levels were observed between $LTA4H^{\Delta hep}$

(F) qPCR detection of *LTA4H* in clinical HCC samples.
(G–J) WB, qPCR, and IHC detection of LTA4H in the DEN-induced mouse HCC model.
(K) ELISA detection of LTB4 in DEN-induced mouse HCC models.
(L) ELISA detection of LTB4 in clinical HCC samples.
(M) Pearson correlation of LTB4 with LTA4H mRNA and protein levels in clinical HCC samples.
(N) Representative images of tumors with low and high LTA4H expression in the TMA HCC cohort.
(O and P) Overall survival (OS) and recurrence-free survival (RFS) according to LTA4H level of patients with HCC in the TMA HCC cohort (n = 133).
(Q and R) Comparison of LTA4H mRNA and protein levels in tumoral and adjacent tissues in the CHCC-HBV cohort.
(S) Pearson correlation of LTA4H mRNA and protein levels in the CHCC-HBV cohort.
(T) OS analysis according to the LTA4H protein level in the CHCC-HBV cohort.
(A, J, and N) Scale bar: 100 μm. (B) Scale bar: 300 μm. (C) p value was calculated by Wilcoxon rank-sum test (n = 133), data represent mean ± SD. (E, F, and L) p value was calculated by paired Wilcoxon signed-rank test (n = 10). (O, P, and T) p value was calculated by log rank test. (H, I, and K) p value was calculated by Student's t test (n = 3), data represent mean ± SD. (Q and R) p value was calculated by Wilcoxon rank-sum test (n = 159), the line and box represent median and upper and lower quartiles, respectively. All the replicates represent biological replicates. See also Tables S1 and S2.

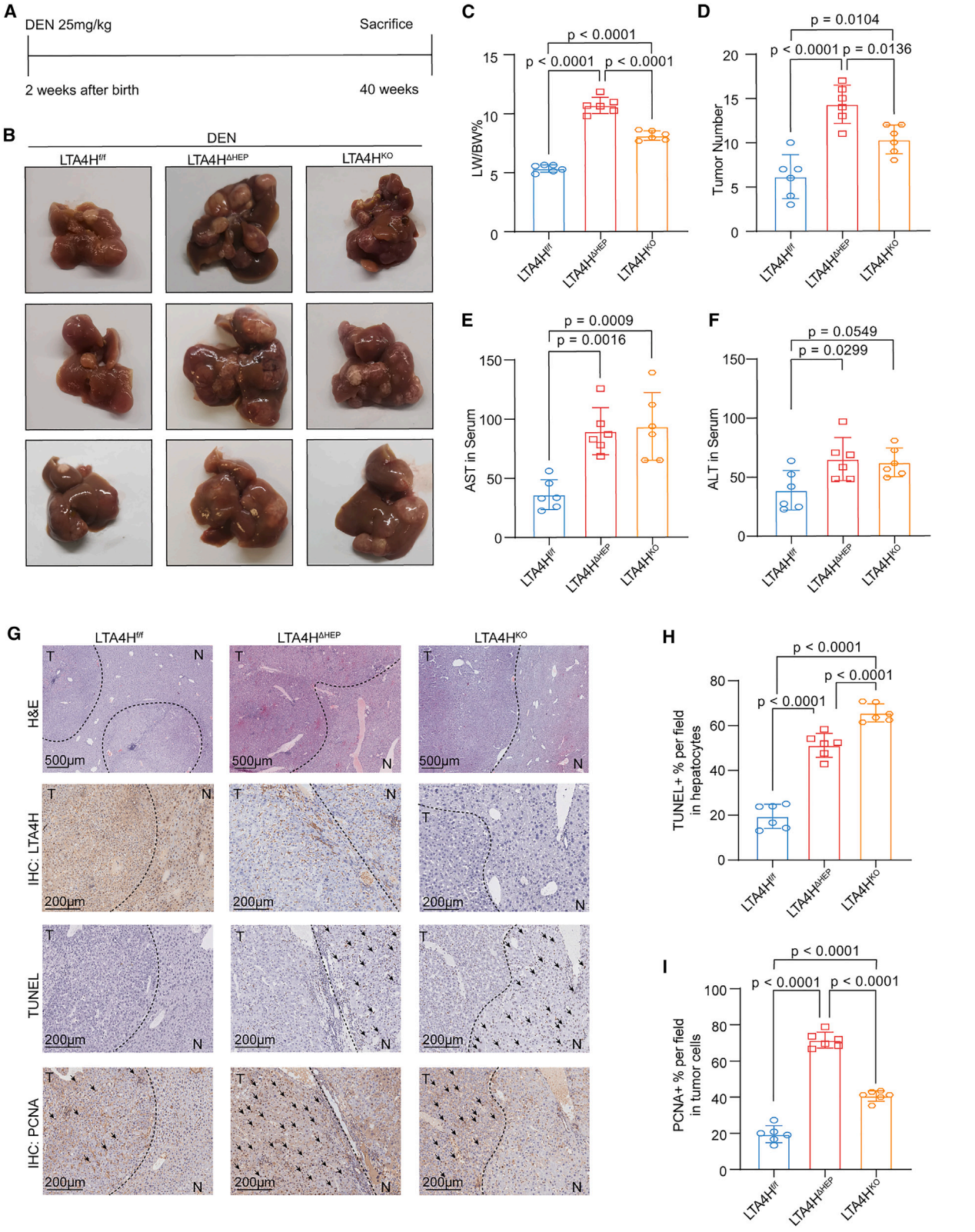

(legend on next page)

and LTA4H^{KO} mice (Figures 2E and 2F). When mice were administered DEN followed by weekly injections of carbon tetrachloride (CCl_4), similar results were observed, consistent with the DEN-induced HCC model (Figures S1B–S1G). Based on these findings, we hypothesized that hepatocyte-specific LTA4H deficiency contributes to liver injury induced by DEN, while LTA4H derived from some stromal cells may influence tumor cell proliferation. To test this hypothesis, IHC of TUNEL and proliferating cell nuclear antigen (PCNA) was performed to quantify damaged and proliferative cells in the liver (Figure 2G). The percentage of TUNEL$^+$ hepatocytes and PCNA$^+$ tumor cells was higher in LTA4H$^{\Delta hep}$ and LTA4H^{KO} mice than in LTA4H$^{f/f}$ mice. However, LTA4H^{KO} mice displayed more TUNEL$^+$ hepatocytes but fewer PCNA$^+$ tumor cells compared to LTA4H$^{\Delta hep}$ mice (Figures 2H and 2I). These findings suggest that LTA4H deficiency exacerbates DEN-induced hepatocytic damage, while LTA4H in some non-parenchymal cells may enhance tumor progression in HCC.

LTA4H ablation mediates hepatocytic damage via reducing JNK signal activation

To investigate the possible role of LTA4H in hepatocytic damage, we isolated primary hepatocytes from LTA4H$^{f/f}$ and LTA4H^{KO} mice without treatment. Bulk RNA was extracted from hepatocytes after 12 h in culture and subjected to RNA sequencing (Figure 3A; Table S3). Kyoto Encyclopedia of Genes and Genomes (KEGG) pathway enrichment analysis showed that genes downregulated in LTA4H^{KO} hepatocytes were enriched in the mitogen-activated protein kinase (MAPK) signaling pathway and erb-b2 receptor tyrosine kinase (ErbB) signaling pathway compared with those in LTA4H$^{f/f}$ hepatocytes (Figure 3B). Cross-activation and feedback mechanism between the MAPK and ErbB signaling pathways have been reported.[15] We first assessed the alterations in the MAPK signaling pathway (JNK, extracellular signal-regulated kinases (ERK), P38) and found that LTA4H knockout (KO) decreased JNK phosphorylation levels but not ERK and P38 phosphorylation levels (Figure 3D). Differentially expressed genes in the ErbB signaling pathway (Figure 3C) were validated by qPCR. epidermal growth factor (*Egf*), epidermal growth factor receptor (*Egfr*), and *Nras* were reduced in LTA4H^{KO} hepatocytes (Figures 3E–3G). These findings underscore basal differences in JNK phosphorylation and gene expression between LTA4H$^{f/f}$ and LTA4H^{KO} hepatocytes. Furthermore, *Egf* and *Egfr* expression levels were also downregulated in the adjacent liver tissues of LTA4H$^{\Delta hep}$ and LTA4H^{KO} mice in the DEN-induced HCC model (Figures 3H–3J).

LTB4, a known promoter of JNK phosphorylation via BLT1 or BLT2 receptors,[10,16] was significantly reduced in both serum and liver tissues of LTA4H$^{\Delta hep}$ and LTA4H^{KO} mice compared to LTA4H$^{f/f}$ mice in the DEN-induced HCC model (Figures S2E and S2F). Interestingly, no substantial differences in LTB4 levels were observed between LTA4H^{KO} and LTA4H$^{\Delta hep}$ mice, suggesting that hepatocytes are the primary source of LTB4 in our model. To elucidate the underlying signal mechanism, hepatocytes were treated with DEN, LTB4, JNK inhibitor (JNK-IN-8), BLT1 inhibitor (U-75302), and BLT2 inhibitor (LY255283). Western blot analyses revealed that LTB4 induced JNK and c-Jun phosphorylation in both LTA4H$^{f/f}$ and LTA4H^{KO} hepatocytes. Inhibition of JNK, BLT1, or BLT2 individually significantly reduced JNK and c-Jun phosphorylation (Figure 3K). Next, hepatocytic damage was evaluated using cell viability (CCK8) assays and the expression of damage-associated molecular pattern molecules (*Il6*, *Il1b*, and *Tnfa*). LTA4H^{KO} hepatocytes exhibited more severe damage than LTA4H$^{f/f}$ hepatocytes. LTB4 treatment reversed the DEN-induced hepatocytic damage, which was partially mitigated by the JNK, BLT1, or BLT2 inhibitors individually (Figures 3L, 3M, S2A, and S2B). We further analyzed *Egf* and *Egfr* levels and found that LTB4 induced their expression in both LTA4H$^{f/f}$ and LTA4H^{KO} hepatocytes, which was prevented by the inhibition of JNK, BLT1, and BLT2 (Figures S2C and S2D). In a DEN-induced HCC model in BLT1^{KO} mice, results were consistent with those observed in LTA4H$^{\Delta hep}$ and LTA4H^{KO} mice (Figures S2G–S2I). BLT1^{KO} hepatocytes also exhibited greater severe hepatocytic damage than wild-type hepatocytes (Figures S2J and S2K). In previous studies, we found that EGF/EGFR could promote JNK phosphorylation,[17] which suggested a potential positive feedback pathway between JNK activation and the EGF/EGFR signaling pathway. In summary, our findings demonstrate a protective role of LTA4H in mitigating hepatocytic damage via JNK activation.

LTA4H deficiency shifts the TME toward high infiltration of M2-like macrophages

The role of LTA4H, a gene that regulates inflammation, in shaping the TME of HCC remains unclear. Tumor samples from LTA4H$^{f/f}$ and LTA4H^{KO} DEN-induced mouse HCC models were analyzed using mass cytometry (CyTOF) to assess the percentage and functional status of immune cells (Figures 4A, 4B, and S3A–S3D; Table S4). Analysis of 29 markers revealed 20 distinct cell clusters, showing increased infiltration of CD206$^+$ macrophages (C14, C16, and C20) and neutrophils (C6), alongside decreased infiltration of CD40$^+$ macrophages (positive CD86 expression, C2 and C11) and programmed death ligand 1 (PD-L1$^+$) dendritic cells (C9) in LTA4H-deficient tumors. The proportions of other immune cell clusters were comparable between LTA4H$^{f/f}$ and LTA4H^{KO} HCC tumors (Figures 4C–4E). The frequency of CD86$^+$ macrophages lacking CD40 expression (C10 and C17)

Figure 2. Hepatocyte-specific LTA4H ablation promotes hepatocarcinogenesis

(A) Scheme of the DEN-induced HCC mouse model.

(B) Gross liver tumor images from LTA4H$^{f/f}$, LTA4H$^{\Delta hep}$, and LTA4H^{KO} mice post DEN treatment.

(C and D) Liver weight/body weight ratios and tumor counts among LTA4H$^{f/f}$, LTA4H$^{\Delta hep}$, and LTA4H^{KO} mice.

(E and F) Serum ALT and AST levels for liver injury evaluation.

(G) H&E, LTA4H, TUNEL, and PCNA staining of mouse liver sections.

(H and I) Comparison of the proportions of TUNEL$^+$ and PCNA$^+$ cells among LTA4H$^{f/f}$, LTA4H$^{\Delta hep}$, and LTA4H^{KO} mice.

(G) H&E image scale bar: 500 μm, IHC image scale bar: 200 μm. (C–F, H, and I) *p* values were calculated by one-way ANOVA with Tukey's multiple comparison analysis ($n = 6$). Data represent mean ± SD. All the replicates represent biological replicates. See also Figure S1.

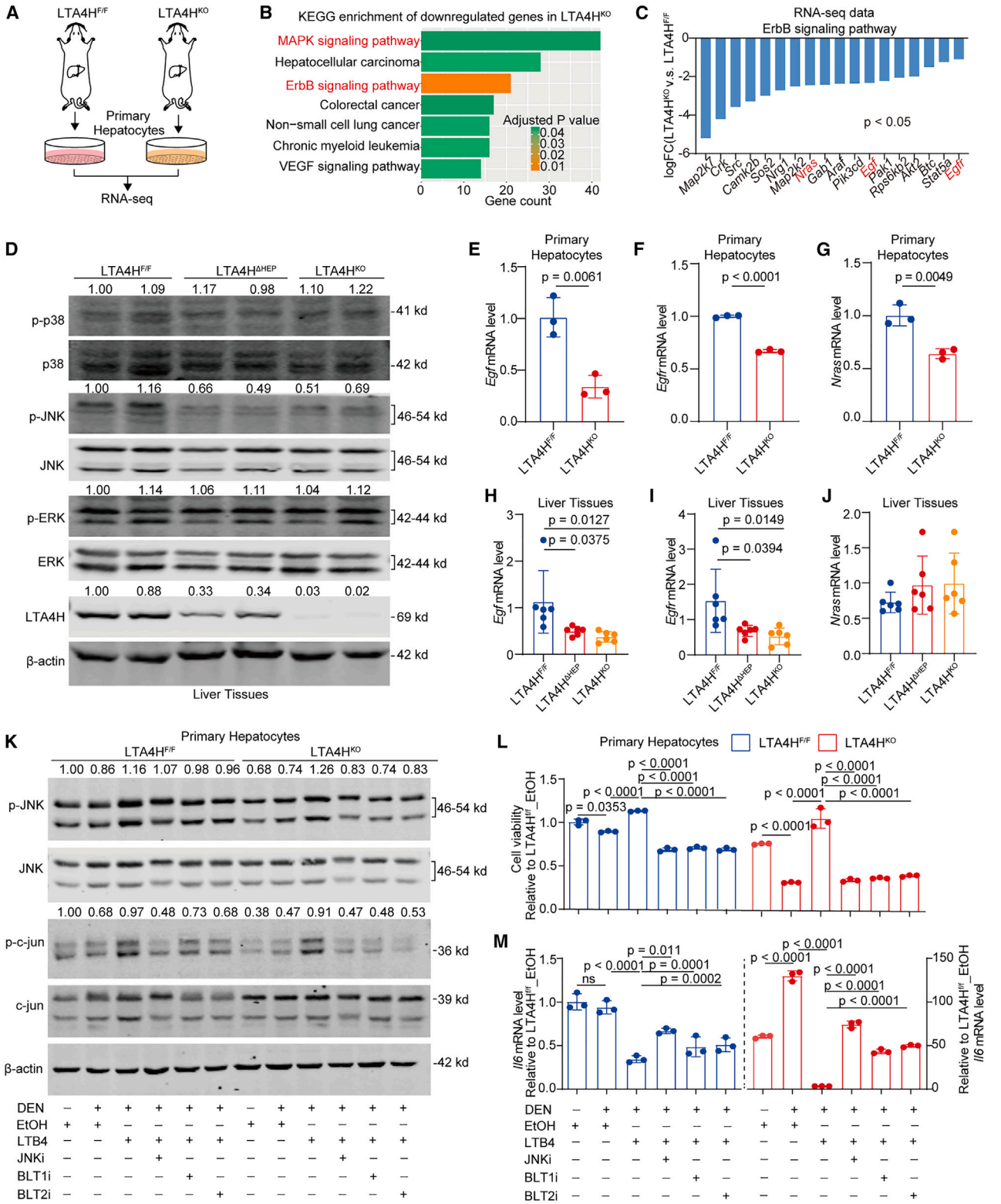

(legend on next page)

remained unchanged between the groups. CD40 has been reported to stimulate antitumorigenic macrophage functions by regulating fatty acid and glutamine metabolism.[18] $CD40^+$ macrophages exhibited opposing differentiation trajectories compared to $CD206^+$ macrophages, as revealed by a diffusion map analysis[19] (Figure 4F). Differential expression of CD206 and PD-L1 suggested that $CD206^+$ macrophages were immunosuppressive M2-like macrophages, whereas $CD40^+$ macrophages (C2 and C11) were M1-like macrophages (Figures 4G, 4H, and S3B). The ratio of $CD206^+$ macrophages to $CD40^+$ macrophages significantly increased in $LTA4H^{KO}$ tumors (Figure 4I). $PD\text{-}L1^+$ dendritic cells exhibited increased expression of CD11b and PD-L1 with decreased CD24 levels, suggesting an immunosuppressive phenotype (Figure S3C).

We confirmed these findings in tumor sections from $LTA4H^{f/f}$, $LTA4H^{\Delta hep}$, and $LTA4H^{KO}$ mice using multiplex IHC (mIHC). While there were no significant differences in $PD\text{-}L1^+$ dendritic cells among the groups, neutrophil infiltration was elevated only in $LTA4H^{KO}$ tumors, indicating a contribution from non-parenchymal LTA4H deficiency to neutrophil infiltration (Figure S3E). $CD206^+$ macrophages and the ratio of $CD206^+$ macrophages to $CD40^+$ macrophages were higher in $LTA4H^{\Delta hep}$ and $LTA4H^{KO}$ mice compared to $LTA4H^{f/f}$ mice. Consistent with the tumor burden variations, $LTA4H^{KO}$ mice showed lower levels of $CD206^+$ macrophages and a reduced ratio of $CD206^+$ macrophages to $CD40^+$ macrophages compared to $LTA4H^{\Delta hep}$ mice (Figures 4J, 4K, and S3F), suggesting that macrophage phenotypic changes play a critical role in LTA4H-ablation-induced hepatocarcinogenesis.

To elucidate *LTA4H* expression in human HCC, the analysis of published single-cell RNA sequencing data[20,21] revealed that myeloid cells were the primary non-parenchymal cells expressing *LTA4H* (Figures S4A–S4D). Bone marrow-derived macrophages (BMDMs) from $LTA4H^{f/f}$ and $LTA4H^{KO}$ mice were polarized to M1 and M2 phenotypes using lipopolysaccharide + interferon-gamma or interleukin-4, respectively. LTA4H deficiency impaired both M1 (*Cxcl9* and *Cxcl10*) and M2 polarization (*Arg1* and *Mrc1*) (Figures S4E–S4H), indicating that LTA4H expression in macrophages is essential for their polarization.

Overall, hepatocyte-specific LTA4H ablation increases the frequency of M2-like macrophages in a mouse HCC model, highlighting its critical role in promoting HCC progression and shaping an immunosuppressive TME.

Hepatocyte-specific LTA4H deficiency promotes M2-like macrophage polarization by upregulating LTBP1 expression and TGF-β secretion

To explore how LTA4H deficiency promotes M2-like macrophage polarization, we examined differentially expressed secretory genes between $LTA4H^{f/f}$ and $LTA4H^{KO}$ hepatocytes (Figure 3A). Nine secreted genes were significantly upregulated in $LTA4H^{KO}$ hepatocytes (Figure 5A), including *Apob*, *Apoe*, *Mmp8*, *Lcn2*, and *Ltbp1*, which have been implicated in M2 macrophage polarization.[22–26] Validation experiments in primary hepatocytes confirmed the upregulation of *Ltbp1* and *Lcn2* in $LTA4H^{KO}$ hepatocytes (Figures 5B and S5A–S5D). Further, *Ltbp1* was upregulated in LTA4H KO liver tissues and Hepa1-6 cells but downregulated in LTA4H-overexpressing Hepa1-6 cells (Figures 5C–5E and S5E–S5G). Protein and mRNA analysis confirmed that LTBP1 was negatively regulated by LTA4H (Figures 5F and 5G). High *LTBP1* expression correlated with poor prognosis in patients from the TGCA-LIHC cohort (Figure S5H).

LTBP1, a member of the latent TGF-β binding protein family, contributes to latent TGF-β secretion and activation. TGF-β plays a pivotal role in HCC progression by promoting M2 macrophage differentiation, which suppresses $CD8^+$ T cells, natural killer cells, and dendritic cell activity and enhances $CD4^+$ regulatory T cell activity.[5] We detected total TGF-β secretion levels in Hepa1-6 cells and found that TGF-β secretion significantly decreased with overexpressing LTA4H and increased with LTA4H KO (Figures 5H and 5I). Both total TGF-β and active TGF-β were elevated in the serum of the $LTA4H^{\Delta hep}$ and $LTA4H^{KO}$ DEN-induced HCC model (Figures 5J and 5K). Notably, *Tgfb* expression remained unchanged between LTA4H-manipulated and control Hepa1-6 cells (Figures S5I and S5J), indicating that LTA4H primarily modulates the secretion and activation of TGF-β.

To test whether LTA4H affects M2-like macrophages via TGF-β, we cocultured BMDMs with conditioned media (CM) from Hepa1-6 cells with or without LTA4H KO. Latent TGF-β in the CM was activated using hydrochloric acid and neutralized with sodium hydroxide (Figure 5L). $LTA4H^{KO}$ CM promoted M2 polarization, which was abolished by TGF-β blockade (Figures 5M–5P). Using mIHC in the TMA HCC cohort, we observed a significant negative correlation between LTA4H and both LTBP1 and $CD206^+CD68^+$ macrophages (Figures 5Q and 5R). LTBP1 expression was elevated in HCC tumors and correlated with

Figure 3. LTA4H ablation mediates hepatocytic damage via reducing JNK signal activation

(A) RNA sequencing scheme for $LTA4H^{f/f}$ and $LTA4H^{KO}$ primary hepatocytes.
(B) KEGG enrichment of downregulated genes in $LTA4H^{KO}$ hepatocytes.
(C) Enriched genes in the ErbB signaling pathway in $LTA4H^{KO}$ hepatocytes.
(D) WB detection of key MAPK signaling molecules (total/phosphorylated p38 MAPK, JNK, and ERK) in $LTA4H^{f/f}$, $LTA4H^{\Delta hep}$, and $LTA4H^{KO}$ adjacent liver tissues from mice HCC models.
(E–G) qPCR analysis of *Egf*, *Egfr*, and *Nras* in $LTA4H^{f/f}$ and $LTA4H^{KO}$ hepatocytes ($n = 3$).
(H–J) Validation of *Egf*, *Egfr*, and *Nras* expression in adjacent liver tissues from $LTA4H^{f/f}$, $LTA4H^{\Delta hep}$, and $LTA4H^{KO}$ mice HCC models ($n = 6$).
(K) Immunoblot of total/phosphorylated JNK and c-Jun in $LTA4H^{f/f}$ and $LTA4H^{KO}$ hepatocytes treated with DEN, ethanol (vehicle of LTB4), LTB4, JNK inhibitor, BLT1 inhibitor, and BLT2 inhibitor as indicated.
(L) Comparison of the viability of $LTA4H^{f/f}$ and $LTA4H^{KO}$ hepatocytes subjected to different treatments ($n = 3$).
(M) qPCR analysis of *Il6* expression in $LTA4H^{f/f}$ and $LTA4H^{KO}$ hepatocytes under various treatments ($n = 3$).
(E–G) *p* values were calculated by Student's t test, data represent mean ± SD. (H–J, L, and M) *p* values were calculated by one-way ANOVA with Tukey's multiple comparison analysis, data represent mean ± SD. All the replicates represent biological replicates. See also Figure S2; Table S3.

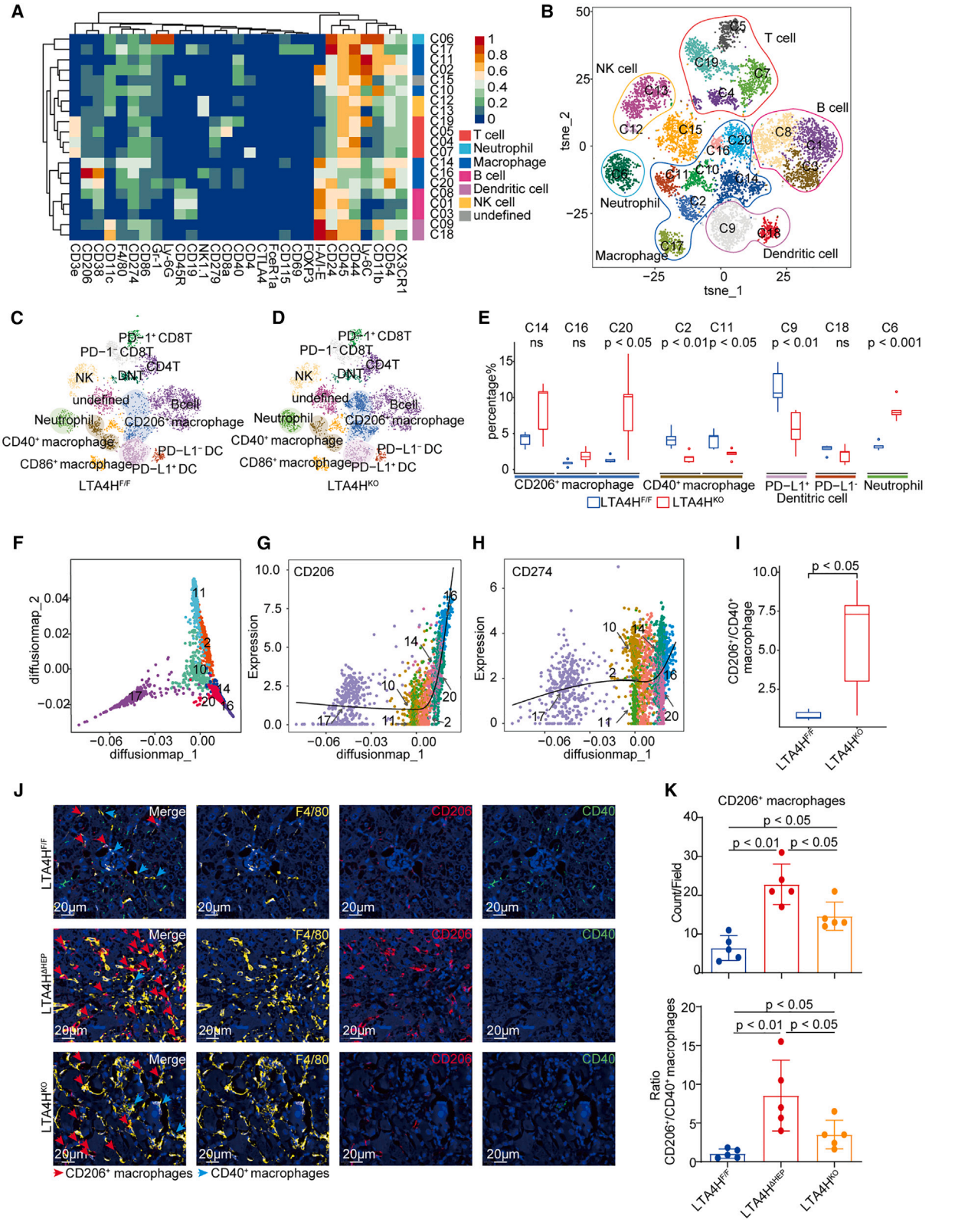

(legend on next page)

poor prognosis (Figures S5K–S5M). Macrophage depletion using clodronate-containing liposomes inhibited tumor progression in the scramble group and abolished tumor enhancement in LTA4H KO tumors (Figures 5S and 5T). Additionally, mIHC revealed that macrophage depletion reversed $CD8^+$ T cell exhaustion and increased the proportion of $GZMB^+CD8^+$ T cells (Figures S6A–S6D). These findings also supported the direct role of M2-like macrophages in mediating the pro-tumorigenic effects of LTA4H deficiency.

Collectively, LTA4H ablation promotes M2-like macrophage polarization through enhancing TGF-β secretion and activation, mediated by LTBP1 upregulation.

LTA4H negatively regulates LTBP1 expression by inhibiting *Ltbp1* mRNA maturation and processing mediated by HNRNPA1

We investigated the molecular mechanism by which LTA4H regulates LTBP1 expression. First, we explored the role of the LTA4H/LTB4/LTB4R pathway in hepatocytes. LTB4 treatment reduced *Ltbp1* levels in both $LTA4H^{f/f}$ and $LTA4H^{KO}$ hepatocytes, which were restored by inhibition of BLT1 or BLT2. Notably, inhibiting BLT1 in $LTA4H^{KO}$ hepatocytes caused a sharper *Ltbp1* increase, suggesting an intrinsic inhibitory mechanism of LTA4H (Figure S7A). Next, we assessed *Ltbp1* mRNA stability and pre-mRNA levels in $LTA4H^{f/f}$ and $LTA4H^{KO}$ hepatocytes, as well as in Hepa1-6 cells with LTA4H overexpression or KO. Results showed no significant differences, indicating that LTA4H might regulate *Ltbp1* expression via mRNA processing rather than transcription and stability (Figures S7B–S7E). Interestingly, nuclear enrichment of LTA4H was observed in human and mouse HCC-adjacent tissues (Figures S7F and S7G). We hypothesized that nuclear enrichment of LTA4H might directly participate in the regulation of mRNA processing and maturation of LTBP1.

Anti-Flag-LTA4H co-immunoprecipitation (coIP) with liquid chromatography-tandem mass spectrometry (LC-MS/MS) identified 46 specific proteins (Figure 6A; Table S5). Enrichment analysis revealed that most of the proteins mainly involved in pathways related to protein-RNA binding and RNA processing and splicing (Figure 6B). Furthermore, Tubulin Alpha 4a (TUBA4A) and HNRNPA1 were identified as potential interactors of LTA4H (Figure 6C). HNRNPA1, also known as heterogeneous nuclear ribonucleoprotein A1, is mainly found in the cell nucleus and is involved in multiple cellular processes, including RNA processing, transport, and localization. Interestingly, *LTBP1* was identified in a dataset of HNRNPA1 splicing targets.[27] Intriguingly, knockdown of HNRNPA1 decreased LTBP1 protein and mRNA levels in Hepa1-6 cells (Figures 6D and 6E). Next, coIP assays confirmed the interaction between LTA4H and HNRNPA1, which was RNA independent (Figures 6F–6K).

RNA immunoprecipitation (RIP)-qPCR revealed that LTA4H overexpression reduced HNRNPA1 binding to *Ltbp1* mRNA (Figure S7H). Because decreased *Ltbp1* levels after LTB4 treatment were observed in $LTA4H^{KO}$ hepatocytes (Figure S7A), we conjectured that LTB4-induced HNRNPA1 phosphorylation might also inhibit HNRNPA1-mediated regulation of *Ltbp1* mRNA processing and maturation. We examined the phosphorylation level of HNRNPA1 in LTA4H KO Hepa1-6 cells treated with LTB4 for various durations. The phosphorylation of HNRNPA1 increased significantly with time in LTA4H KO Hepa1-6 cells (Figure 6L). Moreover, LTB4 treatment prevented the binding of HNRNPA1 and *Ltbp1* mRNA in LTA4H KO Hepa1-6 cells, which suggested that phosphorylation of HNRNPA1 affected its interaction with *Ltbp1* mRNA (Figure 6L). In addition, LTA4H KO Hepa1-6 cells showed greater interaction between HNRNPA1 and *Ltbp1* mRNA than did scramble Hepa1-6 cells in the presence or absence of LTB4, which suggested that the absence of an interaction between LTA4H and HNRNPA1 promoted the binding of HNRNPA1 and *Ltbp1* mRNA (Figure 6L). Furthermore, a decrease in the interaction between HNRNPA1 and *Ltbp1* mRNA also exhibited a time-dependent gradient response to LTB4 treatment in normal Hepa1-6 cells (Figures 6N and 6O). Collectively, these data verified that LTA4H inhibited LTBP1 expression via phosphorylation of HNRNPA1 through LTB4 or direct interaction.

Unexpectedly, LTB4 treatment increased HNRNPA1-LTA4H binding, implying that phosphorylation of HNRNPA1 enhanced their interaction (Figure 6N). Given the lack of a nuclear localization sequence in LTA4H, these findings suggested that upregulated LTA4H might promote HNRNPA1 binding through phosphorylation by LTB4, thereby facilitating its nuclear localization. Indeed, silencing HNRNPA1 prevented LTB4-induced nuclear

Figure 4. LTA4H deficiency shifts the tumor microenvironment of HCC toward high infiltration of M2-like macrophage

(A) Heatmap of 29 markers expression in each cell cluster.

(B) t-distributed stochastic neighbor embedding (t-SNE) plot of CyTOF data from $CD45^+$ cells in $LTA4H^{f/f}$ and $LTA4H^{KO}$ HCC tumors (n = 5), annotated into specific cell types.

(C and D) t-SNE plots showing cell subpopulations with annotations based on differentially expressed markers in $CD45^+$ cells from $LTA4H^{f/f}$ and $LTA4H^{KO}$ HCC tumors.

(E) Proportion of differential cell clusters among $CD45^+$ cells in $LTA4H^{f/f}$ and $LTA4H^{KO}$ HCC tumors.

(F) Diffusion map showing macrophage clusters as a phenotypic continuum.

(G and H) Mean expression of CD206 and CD274 along diffusion component 1.

(I) Ratio comparison of $CD206^+$ to $CD40^+$ macrophages in $LTA4H^{f/f}$ and $LTA4H^{KO}$ HCC tumors.

(J) mIHC staining of F4/80, CD40, and CD206 verifying macrophage infiltration in $LTA4H^{f/f}$, $LTA4H^{\Delta hep}$, and $LTA4H^{KO}$ HCC tissues. Red arrow: $CD206^+$ macrophages; green arrow: $CD40^+$ macrophages. Scale bar: 20 μm.

(K) Quantification of $CD206^+$ macrophages and the $CD206^+/CD40^+$ macrophage ratio in $LTA4H^{f/f}$, $LTA4H^{\Delta hep}$, and $LTA4H^{KO}$ HCC tumors.

(E) The p value was calculated by Wilcoxon rank-sum test with Benjamini-Hochberg adjustment (n = 5), the line and box represent median and upper and lower quartiles, respectively. (I) The p value was calculated by Wilcoxon rank-sum test (n = 5), the line and box represent median and upper and lower quartiles, respectively. (K) p values were calculated by one-way ANOVA with Tukey's multiple comparison analysis (n = 5), data represent mean ± SD. All the replicates represent biological replicates. See also Figures S3 and S4; Table S4.

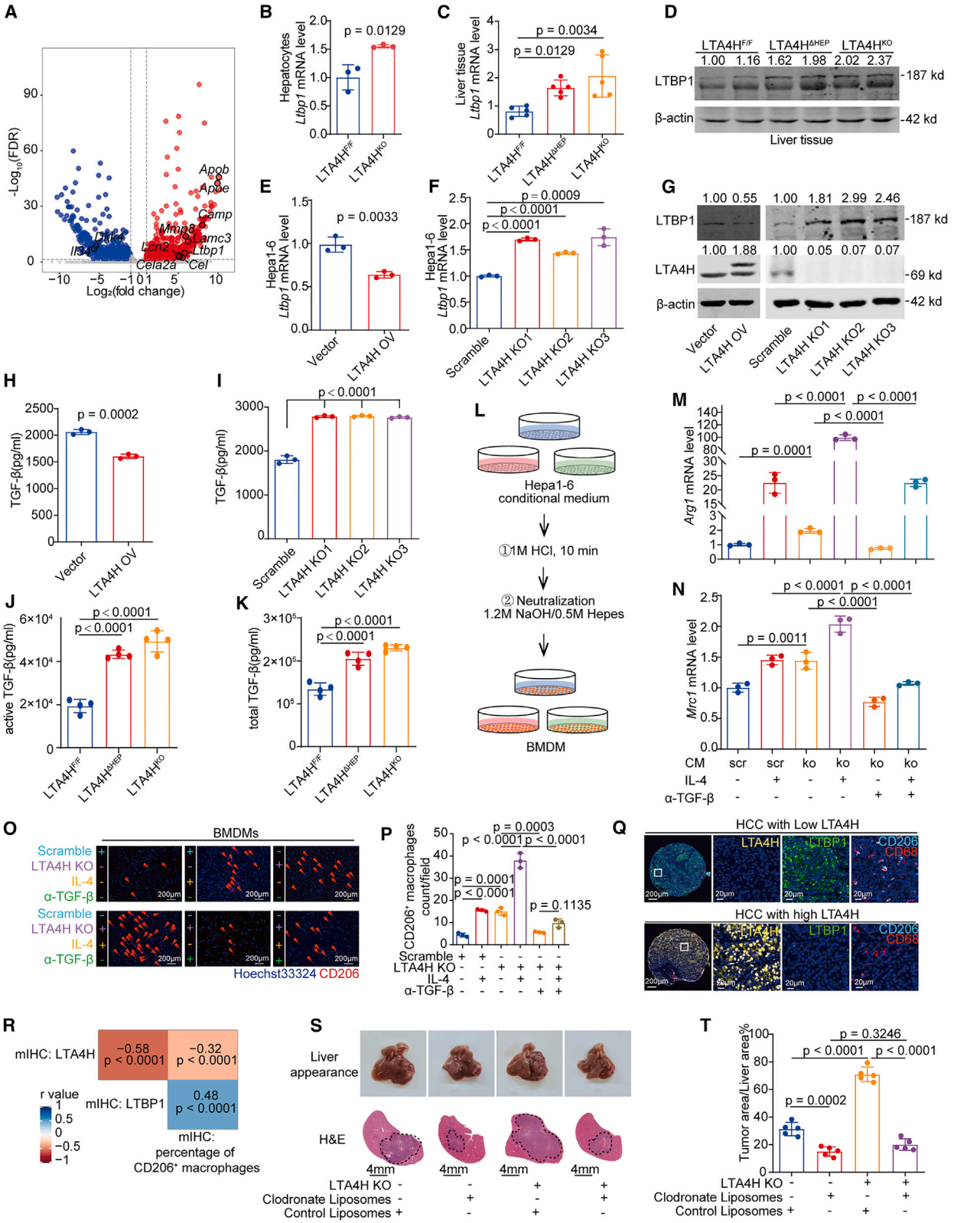

(legend on next page)

translocation of LTA4H (Figures S7I and S7J). BLT1 inhibition, but not BLT2, prevented LTB4-induced nuclear localization of LTA4H (Figures 6P, S7K, and S7L). Additionally, *Hnrnpa1* knockdown reversed LTA4H ablation- or BLT1 inhibition-induced LTBP1 upregulation (Figures S7M and 6Q). In the orthotopic HCC mouse model, *Hnrnpa1* or *Ltbp1* knockdown significantly hindered tumor progression induced by LTA4H deficiency (Figures 6R and S7N–S7P). The mIHC showed that *Hnrnpa1* or *Ltbp1* knockdown inhibited $CD206^+F4/80^+$ macrophage polarization, promoted $CD8^+$ T cell infiltration, decreased the proportion of $PD\text{-}1^+CD8^+$ T cells (PD-1: programmed cell death protein 1), and increased the proportion of $GZMB^+CD8^+$ T cells in LTA4H KO tumors (Figures S8A–S8E).

In summary, LTA4H inhibits HNRNPA1-mediated LTBP1 by facilitating HNRNPA1 phosphorylation through LTB4 or direct interaction. Moreover, LTA4H promotes its own nuclear localization through HNRNPA1.

TGF-β blockade potentiates the efficacy of anti-PD-1 therapy in LTA4H KO tumor-bearing mice

The aforementioned findings drove us to investigate whether disrupting the immunosuppressive crosstalk between tumor cells and macrophages by blocking TGF-β improves anti-PD-1 therapy efficacy in HCC. We constructed an orthotopic HCC mouse model using Hepa1-6 scramble or LTA4H KO cells and treated the mice with anti-PD-1, anti-TGF-β, or a combination of both on day 5 post transplantation. Significant tumor reduction was observed in Hepa1-6 scramble tumors treated with anti-PD-1 therapy or combination therapy, but LTA4H KO tumors showed resistance to anti-PD-1 monotherapy. Combination therapy significantly restricted tumor growth in LTA4H KO tumors compared to IgG or monotherapies (Figures 7A–7F). The mIHC analysis showed that anti-PD-1 monotherapy failed to induce $GZMB^+CD8^+$ T cells and $CD8^+$ T cell infiltration in LTA4H KO tumors, likely due to abundance of $CD206^+$ macrophages. Anti-TGF-β reduced $CD206^+$ macrophages, but only combination therapy simultaneously and effectively decreased the proportion of $PD\text{-}1^+CD8^+$ T cells, increased the proportion of $GZMB^+CD8^+$ T cells, and promoted $CD8^+$ T cell infiltration in LTA4H KO tumors (Figures 7G–7K. This explains the limited efficacy of anti-TGF-β monotherapy in LTA4H KO models, likely due to the pre-existing immunosuppressive microenvironment driving $CD8^+$ T cell exhaustion prior to treatments.

In addition, to investigate whether this finding can be extrapolated to clinical HCC, we analyzed the correlation between the LTA4H level in tumor cells and treatment response in patients with HCC receiving ICIs (ICI cohort, Table S6). Responders exhibited significantly higher LTA4H levels and fewer $CD206^+$ macrophages than non-responders (Figures 7L–7N). These findings suggest LTA4H as a potential biomarker for guiding HCC ICI treatment. Collectively, LTA4H deficiency exacerbated DEN-induced liver damage, while M2-like macrophages driven by TGF-β accumulation from LTA4H-deficient hepatocytes or tumor cells promoted HCC progression. Our study highlights the regulatory role of LTA4H in the TME of HCC through the LTA4H/HNRNPA1/LTBP1/TGF-β axis. Anti-TGF-β may serve as an effective strategy to sensitize LTA4H-deficient patients with HCC to ICIs.

Decreased acetyl-CoA and increased HDAC1 were the main causes of reduced LTA4H expression in HCC

To explore the molecular mechanism of LTA4H downregulation in HCC, we analyzed the CHCC-HBV cohort[13] to identify proteins correlated with LTA4H expression and conducted pathway enrichment analyses (Table S7). Proteins positively correlated with LTA4H were notably enriched in histone deacetylases (HDACs) and acetyltransferase-related pathways (Figure S9A). Histone deacetylation, which increases chromatin compaction, typically suppresses gene transcription. Given the reported decrease in acetyl-CoA synthesis in HCC,[28] we speculated that LTA4H downregulation is linked to histone deacetylation dysfunction. Trichostatin-A (TSA) and nicotinamide treatment enhanced the expression of *Lta4h* mRNA, with acetyl-CoA replenishing reagent (AAR) further augmenting this effect (Figure S9B). Notably, TSA treatment alone significantly induced LTA4H expression, implicating HDACs as key regulators. The combination of AAR and TSA further boosted LTA4H expression compared to TSA alone (Figures S9C and S9D). Analysis of the The Cancer Genome Atlas-Liver Hepatocellular Carcinoma (TCGA-LIHC) database and the CHCC-HBV cohort revealed

Figure 5. Hepatocyte-specific LTA4H deficiency promotes M2-like macrophage polarization by upregulating LTBP1 expression and TGF-β secretion

(A) Volcano plot of differentially expressed and secreted genes in $LTA4H^{KO}$ vs. $LTA4H^{f/f}$ hepatocytes (Figure 3A).
(B) Transcript level of *Ltbp1* in $LTA4H^{f/f}$ and $LTA4H^{KO}$ hepatocytes ($n = 3$).
(C and D) mRNA and protein levels of LTBP1 in liver tissues of $LTA4H^{f/f}$, $LTA4H^{\Delta hep}$, and $LTA4H^{KO}$ mice ($n = 5$).
(E–G) mRNA and protein levels of LTBP1 in Hepa1-6 cells with LTA4H overexpression or knockout ($n = 3$).
(H and I) ELISA for secreted TGF-β in supernatants of Hepa1-6 cells with LTA4H overexpression or knockout ($n = 3$).
(J and K) ELISA for active and total TGF-β serum levels in $LTA4H^{f/f}$, $LTA4H^{\Delta hep}$, and $LTA4H^{KO}$ DEN-induced HCC models ($n = 4$).
(L) The coculture model of BMDMs and CM from scramble or LTA4H KO Hepa1-6 cells, CM pretreated with HCl/NaOH.
(M and N) Transcript levels of *Arg1* and *Mrc1* in BMDMs under different treatments ($n = 3$).
(O) CD206 immunofluorescence in BMDMs from coculture system under various treatments. Scale bar: 200 μm.
(P) Quantification of $CD206^+$ macrophage in BMDMs from coculture system under various treatments ($n = 3$).
(Q) mIHC staining for LTA4H, LTBP1, CD206, and CD68 in HCC tissues with low or high LTA4H expression from the TMA HCC cohort. Scale bar: 200 μm, enlarged images scale bar: 20 μm.
(R) Quantification and Pearson correlation among LTA4H, LTBP1, and $CD206^+$ macrophages in the TMA HCC cohort.
(S) Liver images and H&E staining of orthotopic HCC tumors (Hepa1-6 scramble and LTA4H KO) with or without macrophage depletion. Scale bar: 4 mm.
(T) Tumor burden comparison across groups, determined by tumor-to-liver area ratio in sections ($n = 5$).
(B, E, and H) *p* value was calculated by Student's t test, data represent mean ± SD. (C, F, I–K, M, N, P, and T) *p* values were calculated by one-way ANOVA with Tukey's multiple comparison analysis, data represent mean ± SD. All the replicates represent biological replicates. See also Figures S5 and S6.

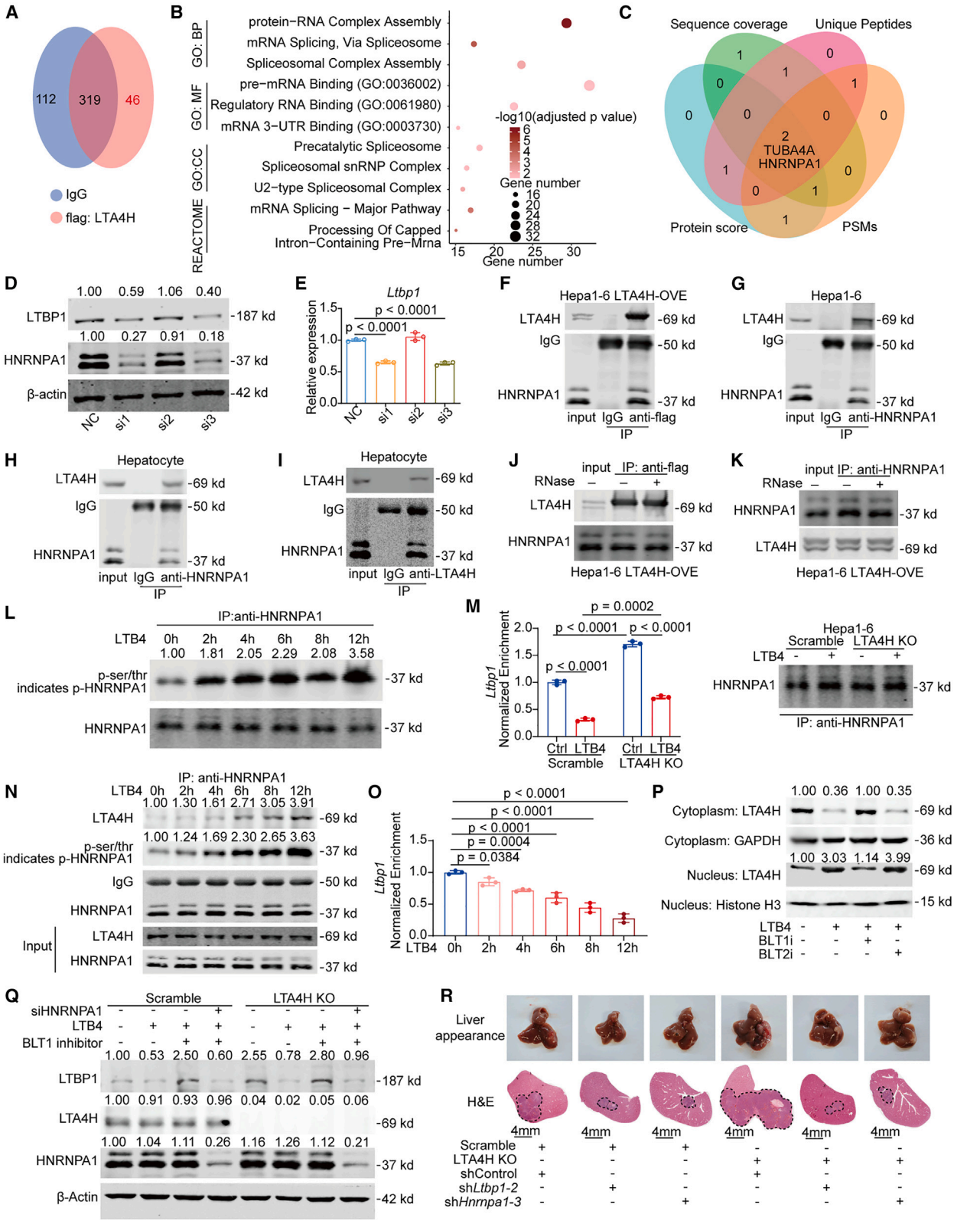

(legend on next page)

elevated HDAC1 and HDAC2 expression in HCC, correlating with poor prognosis (Figures S9E–S9H and S10A–S10D). LTA4H negatively correlated with HDAC1 and HDAC2 in the CHCC-HBV cohort (Figures S10H and S10I). Knockdown experiments in Hepa1-6 cells showed that silencing HDAC1, but not HDAC2, significantly increased LTA4H transcript and protein levels (Figures S9I–S9K and S10E–S10G). Analysis of our clinical HCC samples and TMA HCC cohort corroborated these findings (Figures S9P–S9T, S10J, and S10K). Using regulatory potential score from CistromeDB, we identified a strong association between H3K27ac modification and LTA4H expression (Figures S10L and S10M). Given HDAC1's role in deacetylating H3K27ac,[29] chromatin immunoprecipitation sequencing (ChIP-seq) analysis confirmed that HDAC1 silencing promoted H3K27ac accumulation at the LTA4H promoter (Figures S9U and S9V), a result further validated by ChIP-qPCR (Figures S9W and S9X). These findings suggest that reduced acetyl-CoA levels and elevated HDAC1 expression suppress LTA4H expression by inhibiting H3K27ac modification at its promoter in HCC.

DISCUSSION

LTA4H has been implicated in promoting tumor progression in cancers like skin, colorectal, and ovarian cancers by enhancing cell proliferation and metastasis. Additionally, it contributes to inflammation in lung diseases such as emphysema through Proline-Glycine-Proline (PGP) degradation and LTA4-to-LTB4 conversion, critical for neutrophil and macrophage recruitment.[8,30] However, its role in reshaping the TME remains underexplored. Recent findings in ovarian cancer suggest that LTA4H may foster an immunosuppressive TME via CCL5.[11] In this study, we found that LTA4H ablation correlates with HCC occurrence and immunotherapy response. LTA4H ablation exacerbated liver damage and fostered M2-like macrophage infiltration in HCC. We identified TGF-β-dependent M2-like polarization as a mechanism by which LTA4H deficiency drives HCC progression.

Metabolic enzymes have been shown to regulate nuclear gene expression, as seen with pyruvate dehydrogenase's role in histone acetylation.[31] Here, we revealed that LTA4H regulated LTBP1 expression and TGF-β secretion and activation through nuclear mechanisms. LTA4H interacts with HNRNPA1, a process enhanced by LTB4-induced HNRNPA1 phosphorylation, which disrupts HNRNPA1 binding to *Ltbp1* mRNA, inhibiting *Ltbp1* mRNA processing. Given LTBP1's role in TGF-β signaling,[32–35] highly activated TGF-β signaling contributes to an exhausted TME and poor PD-1 blockade response in HCC. Functional studies showed that TGF-β blockade reversed immune suppression in LTA4H-deficient tumors, highlighting TGF-β inhibition as a promising strategy to enhance ICI efficacy.[5,36,37]

Therapies combining macrophage-targeting drugs with ICIs are emerging in HCC treatment. Clinical trials demonstrate the potent antitumor effects of blockade of TGF-β or its receptor across various cancers, including HCC, with an acceptable safety profile.[38] Recent advancements involved the combination of anti-TGF-β antibodies or receptor inhibitors (galunisertib) with ICIs, which triggered robust antitumor immunity and tumor regression in a mouse model.[39] M7824, a bifunctional fusion protein targeting PD-L1 and TGF-β, was developed to activate innate and adaptive immune responses and induce tumor regression in mouse models.[40] Our findings supported TGF-β inhibition to improve ICI outcomes in LTA4H-deficient HCC. Additionally, our ICI cohort revealed that non-responders to ICIs exhibited significantly lower LTA4H expression, suggesting LTA4H as a predictive biomarker for immunotherapy response.

We also identified key factors underlying LTA4H dysregulation in HCC, including reduced acetyl-CoA levels and elevated HDAC1 expression, which impair histone acetylation at the *LTA4H* promoter. Low levels of acetyl-CoA and high expression of HDAC1, which are the main causes of the dysregulation of histone acetylation, have been reported in HCC.[28,41] Given the absence of a nuclear localization sequence in LTA4H, we found that the nuclear translocation of LTA4H depended on HNRNPA1. Given the enrichment of LTA4H-binding proteins associated with mRNA splicing, more functions and mechanisms of nuclear LTA4H need to be further studied.

In summary, LTA4H deficiency in HCC cells promotes TGF-β secretion and activation, and M2-like macrophage programming and immune escape. Our study underscores the potential of LTA4H as a biomarker for ICI response and highlights TGF-β inhibition to enhance therapeutic outcomes in LTA4H-deficient HCC.

Figure 6. LTA4H negatively regulates LTBP1 expression by inhibiting *Ltbp1* mRNA maturation and processing mediated by HNRNPA1

(A) Venn diagram of proteins identified via anti-IgG and anti-Flag immunoprecipitation-mass spectrometry (IP-MS).
(B) Gene Ontology (GO) and Reactome pathway analyses of 46 potential LTA4H-binding proteins.
(C) Venn diagram of top LTA4H-binding candidates.
(D and E) WB and qPCR for LTBP1 and HNRNPA1 expression in Hepa1-6 with *Hnrnpa1* knockdown.
(F and G) Reciprocal IP validated LTA4H-HNRNPA1 interaction in Hepa1-6 cells.
(H and I) Reciprocal IP validated LTA4H-HNRNPA1 interaction in primary hepatocytes.
(J and K) coIP tested LTA4H-HNRNPA1 interaction in LTA4H-overexpressing Hepa1-6 cells with or without RNaseA/T1 treatment.
(L) Endogenous HNRNPA1 phosphorylation assessed via WB after coIP in LTA4H KO Hepa1-6 cells treated with LTB4 for various durations.
(M) RIP-PCR validated HNRNPA1 and *Ltbp1* mRNA interaction after LTB4 treatment in Hepa1-6 cells with or without LTA4H knockout.
(N) coIP tested LTA4H-HNRNPA1 interaction in Hepa1-6 cells over time under LTB4 treatment.
(O) RIP-PCR verified HNRNPA1-*Ltbp1* mRNA interaction in cells described in (N).
(P) LTA4H distribution was examined in nuclear and cytoplasmic extracts from Hepa1-6 cell with different treatments.
(Q) WB examined the effects of LTB4, BLT1 inhibitor, and HNRNPA1 knockdown on LTBP1 expression in Hepa1-6 scramble and LTA4H KO cells.
(R) Liver images and H&E staining of Hepa1-6 scramble and LTA4H KO orthotopic HCC tumors with *Hnrnpa1* or *Ltbp1* knockdown ($n = 5$). Scale bar: 4 mm.
(E, M, and Q) p values were calculated by one-way ANOVA with Tukey's multiple comparison analysis ($n = 3$), data represent mean ± SD. All the replicates represent biological replicates. See also Figures S7 and S8; Table S5.

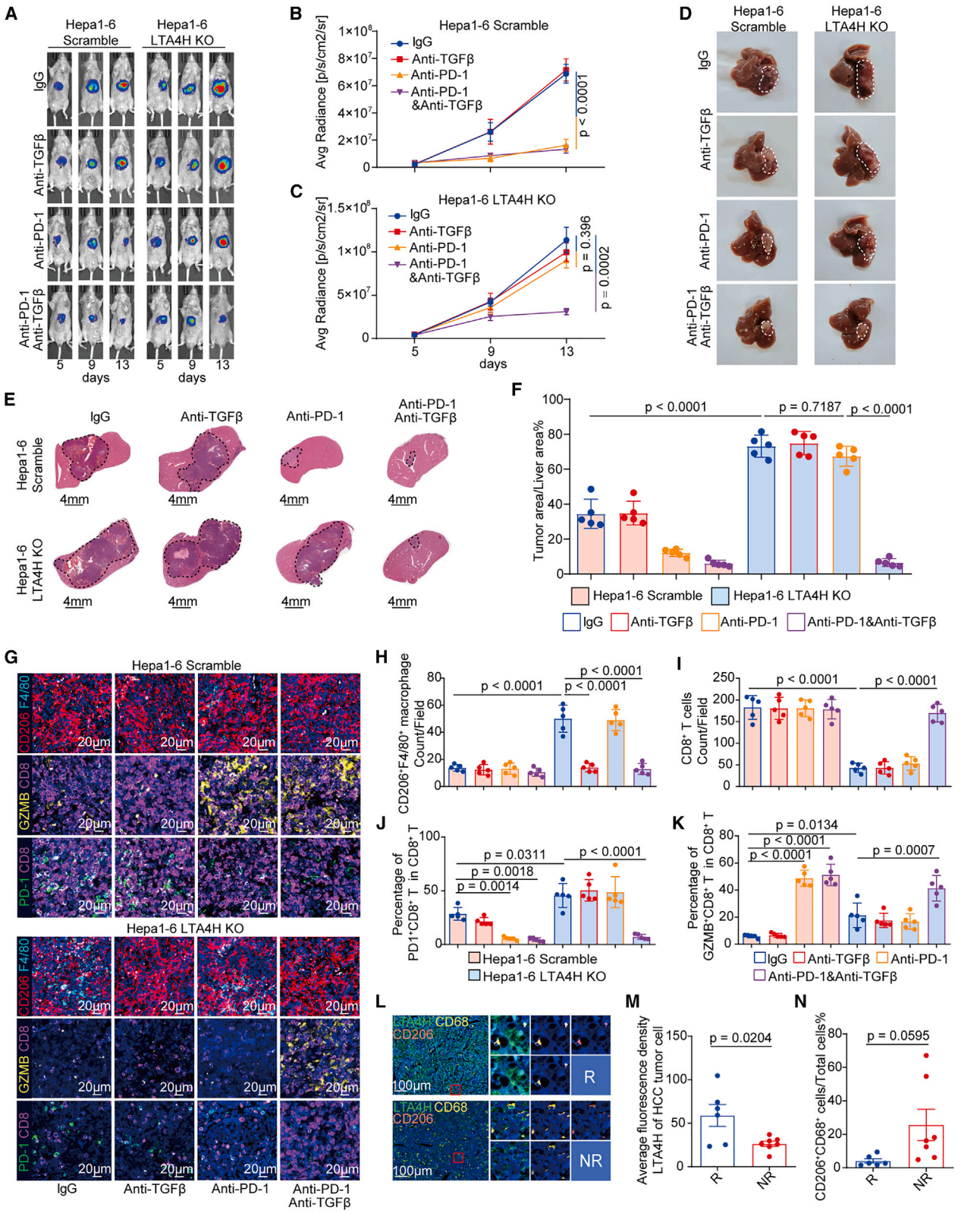

(legend on next page)

Limitations of the study

This study systematically elucidates the role and mechanism of LTA4H in HCC progression via targeting the HNRNPA1/LTBP1/TGF-β axis. However, there are some limitations. In the macrophage depletion experiment, clodronate-containing liposomes were used to deplete all macrophages. While widely applied in studies of TAMs, this approach does not directly address the $CD206^+$ macrophage dependency of LTA4H in tumor progression. Additionally, we identified a strong association between LTA4H and mRNA splicing through its interaction with HNRNPA1, but further investigation is needed to fully understand the broader functions and mechanisms of nuclear LTA4H. We focused on investigating the role of LTA4H in hepatocytes and tumor cells during HCC progression. However, given its expression in immune cells, particularly macrophages, the function of LTA4H in these cells warrants further exploration in future studies.

RESOURCE AVAILABILITY

Lead contact

Further information and requests for resources and reagents should be directed to and will be fulfilled by the lead contact, Lei Chen (chenlei@smmu.edu.cn).

Materials availability

All materials used in this study are available from the lead contact without restriction.

Data and code availability

Raw transcriptome sequencing data (in fastq format) are available on NGDC_SRA with accession number CRA022579 (NGDC: CRA022579). Raw data (.fcs) of mass cytometry were deposited in FlowRepository (FlowRepository: FR-FCM-Z7W7, http://flowrepository.org/id/RvFrwdQZoBHMmZfhB4OY9X5wuLKDYIOF2ILVOSyjSoFd2XrTNexN54bulKjFlvwm). Raw LC-MS/MS data are available via ProteomeXchange with identifier PXD060326 (ProteomeXchange: PXD060326). Raw ChIP-seq data are available on NGDC (NGDC: CRA021482). This paper does not report original code. Any additional information required to reanalyze the data reported in this paper is available from the lead contact upon request.

ACKNOWLEDGMENTS

This work was supported by grants from the National Key R&D Program of China (2022YFC3400903 and 2023YFC2507500), the National Natural Science Foundation of China (82425038, 82421005, U21A20376, 82002921, 82372872, 82273277, and 81988101), and the National Science Foundation of Shanghai (21XD1404600, 21JC1406600, 22140901000, and 21DZ2291900). We thank the project supported by the Shanghai Municipal Science and Technology Major Project.

AUTHOR CONTRIBUTIONS

S.Y., X.Q., and Jing Wu performed most of the experiments. S.Y. and X.Q. performed bioinformatics analysis. Jing Wu, B.Z., Yangqianwen Zhang, and S.L. provided technical assistance for mouse experiments. Y.Y. and S.W. provided clinical samples and performed associated analyses. T.Z. and Yani Zhang provided technical assistance for RNA sequencing. Jianmin Wu, M. Bai, and Z.Z. collected clinical information of TMA. Y.W., J.B., and M.W. provided technical assistance for mIHC and coIP. D.X. and M. Bao collected the samples with immunotherapies. J.H. and S.S. provided technical assistance for mass cytometry. S.Y. wrote the manuscript. L.C. and H.W. provided guidance on the progress of the project and revised the manuscript. All authors have read and approved the article.

DECLARATION OF INTERESTS

H.W., S.Y., and L.C. are inventors on a provisional China patent application related to this work (serial no. 202410654363.0, filed on 24 May 2024).

STAR★METHODS

Detailed methods are provided in the online version of this paper and include the following:

- KEY RESOURCES TABLE
- EXPERIMENTAL MODEL AND STUDY PARTICIPANT DETAILS
  - Tissue microarray and patients
  - Mice and HCC mouse model
  - Isolation and treatment of primary hepatocytes
  - Isolation of bone marrow-derived macrophages (BMDMs) and coculture with conditioned medium
  - Cell lines culture and treatment
- METHOD DETAILS
  - Mass cytometry and analyses
  - H&E and immunohistochemistry
  - Co-IP and LC-MS/MS proteomic assays
  - Western blot
  - Generation of LTA4H KO Hepa1-6 cell lines using CRISPR/Cas9
  - Multiplex immunohistochemistry (mIHC)
  - Quantitative real-time PCR (qPCR)
  - ELISA of total TGF-β and active TGF-β
  - AST and ALT assays
  - RNA sequencing and analysis
  - Nucleocytoplasmic separation

Figure 7. TGF-β blockade potentiates the efficacy of anti-PD-1 therapy in LTA4H knockout tumor-bearing mice

(A) Tumor progression was monitored at 5, 9, and 13 days post inoculation using live bioluminescent imaging in mice injected with scramble or LTA4H KO Hepa1-6 cells and treated with IgG or blocking antibody as indicated.

(B and C) Quantification of the liver tumor burden from live bioluminescent imaging studies.

(D) Images of orthotopic HCC tumors from the indicated treatment groups.

(E) H&E staining of Hepa1-6 orthotopic HCC tumors from treatment groups. Scale bar: 4 mm.

(F) Comparison of tumor burden (tumor area/whole liver area) in orthotopic HCC tumors.

(G) mIHC staining of $CD206^+$ macrophages, PD-1^+CD8^+ T cells, and $GZMB^+CD8^+$ T cells in Hepa1-6 scramble and LTA4H KO orthotopic HCC tumors with the indicated treatments. Scale bar: 20 μm.

(H–K) Comparison of $CD206^+$ macrophages, $CD8^+$ T cells, PD-1^+CD8^+ T cells, and $GZMB^+CD8^+$ T cells among Hepa1-6 scramble and LTA4H KO orthotopic HCC tumors with the indicated treatments.

(L) mIHC staining of LTA4H, CD68, and CD206 in human HCC samples with varying responses to ICIs. Scale bar: 100 μm.

(M and N) Comparison of LTA4H expression in HCC tumor cells and the percentage of $CD206^+$ macrophages between responders ($n = 6$) and non-responders ($n = 7$).

(B, C, F, and H–K) p values were calculated by one-way ANOVA with Tukey's multiple comparison analysis ($n = 5$), data represent mean ± SD. (M and N) p value was calculated by Wilcoxon rank-sum test, data represent mean ± SD. All the replicates represent biological replicates. See also Table S6.

- Immunofluorescence
- RNA immunoprecipitation (RIP)
- RNA stability assay
- Transient knockdown using siRNA
- Chromatin immunoprecipitation
- CHIP-seq analysis

- QUANTIFICATION AND STATISTICAL ANALYSIS

SUPPLEMENTAL INFORMATION

Supplemental information can be found online at https://doi.org/10.1016/j.xcrm.2025.102000.

Received: June 7, 2024
Revised: December 30, 2024
Accepted: February 12, 2025
Published: March 7, 2025

REFERENCES

1. Singal, A.G., Kanwal, F., and Llovet, J.M. (2023). Global trends in hepatocellular carcinoma epidemiology: implications for screening, prevention and therapy. Nat. Rev. Clin. Oncol. *20*, 864–884. https://doi.org/10.1038/s41571-023-00825-3.
2. Llovet, J.M., Pinyol, R., Yarchoan, M., Singal, A.G., Marron, T.U., Schwartz, M., Pikarsky, E., Kudo, M., and Finn, R.S. (2024). Adjuvant and neoadjuvant immunotherapies in hepatocellular carcinoma. Nat. Rev. Clin. Oncol. *21*, 294–311. https://doi.org/10.1038/s41571-024-00868-0.
3. Yang, X., Yang, C., Zhang, S., Geng, H., Zhu, A.X., Bernards, R., Qin, W., Fan, J., Wang, C., and Gao, Q. (2024). Precision treatment in advanced hepatocellular carcinoma. Cancer. Cell. *42*, 180–197. https://doi.org/10.1016/j.ccell.2024.01.007.
4. Hou, J., Zhang, H., Sun, B., and Karin, M. (2020). The immunobiology of hepatocellular carcinoma in humans and mice: Basic concepts and therapeutic implications. J. Hepatol. *72*, 167–182. https://doi.org/10.1016/j.jhep.2019.08.014.
5. Chen, J., Gingold, J.A., and Su, X. (2019). Immunomodulatory TGF-β Signaling in Hepatocellular Carcinoma. Trends Mol. Med. *25*, 1010–1023. https://doi.org/10.1016/j.molmed.2019.06.007.
6. Zhou, C., Weng, J., Liu, C., Liu, S., Hu, Z., Xie, X., Gao, D., Zhou, Q., Sun, J., Xu, R., et al. (2023). Disruption of SLFN11 Deficiency-Induced CCL2 Signaling and Macrophage M2 Polarization Potentiates Anti-PD-1 Therapy Efficacy in Hepatocellular Carcinoma. Gastroenterology *164*, 1261–1278. https://doi.org/10.1053/j.gastro.2023.02.005.
7. Lau, D., Bobe, A.M., and Khan, A.A. (2019). RNA Sequencing of the Tumor Microenvironment in Precision Cancer Immunotherapy. Trends Cancer *5*, 149–156. https://doi.org/10.1016/j.trecan.2019.02.006.
8. Vo, T.T.L., Jang, W.J., and Jeong, C.H. (2018). Leukotriene A4 hydrolase: an emerging target of natural products for cancer chemoprevention and chemotherapy. Ann. N. Y. Acad. Sci. *1431*, 3–13. https://doi.org/10.1111/nyas.13929.
9. Oi, N., Yamamoto, H., Langfald, A., Bai, R., Lee, M.-H., Bode, A.M., and Dong, Z. (2017). LTA4H regulates cell cycle and skin carcinogenesis. Carcinogenesis *38*, 728–737. https://doi.org/10.1093/carcin/bgx049.
10. Zhao, S., Yao, K., Li, D., Liu, K., Jin, G., Yan, M., Wu, Q., Chen, H., Shin, S.H., Bai, R., et al. (2019). Inhibition of LTA4H by bestatin in human and mouse colorectal cancer. EBioMedicine *44*, 361–374. https://doi.org/10.1016/j.ebiom.2019.05.008.
11. Guo, Z., Huang, J., Huo, X., Huang, C., Yu, X., Sun, Y., Li, Y., He, T., Guo, H., Yang, J., and Xue, L. (2024). Targeting LTA4H facilitates the reshaping of the immune microenvironment mediated by CCL5 and sensitizes ovarian cancer to Cisplatin. Sci. China Life Sci. *67*, 1226–1241. https://doi.org/10.1007/s11427-023-2444-5.
12. Oi, N., Jeong, C.-H., Nadas, J., Cho, Y.-Y., Pugliese, A., Bode, A.M., and Dong, Z. (2010). Resveratrol, a red wine polyphenol, suppresses pancreatic cancer by inhibiting leukotriene A_4hydrolase. Cancer Res. *70*, 9755–9764. https://doi.org/10.1158/0008-5472.CAN-10-2858.
13. Gao, Q., Zhu, H., Dong, L., Shi, W., Chen, R., Song, Z., Huang, C., Li, J., Dong, X., Zhou, Y., et al. (2019). Integrated Proteogenomic Characterization of HBV-Related Hepatocellular Carcinoma. Cell *179*, 1240. https://doi.org/10.1016/j.cell.2019.10.038.
14. Lee, T.H., Kim, W.R., Benson, J.T., Therneau, T.M., and Melton, L.J. (2008). Serum aminotransferase activity and mortality risk in a United States community. Hepatology *47*, 880–887. https://doi.org/10.1002/hep.22090.
15. Burotto, M., Chiou, V.L., Lee, J.-M., and Kohn, E.C. (2014). The MAPK pathway across different malignancies: a new perspective. Cancer *120*, 3446–3456. https://doi.org/10.1002/cncr.28864.
16. He, R., Chen, Y., and Cai, Q. (2020). The role of the LTB4-BLT1 axis in health and disease. Pharmacol. Res. *158*, 104857. https://doi.org/10.1016/j.phrs.2020.104857.
17. Lanaya, H., Natarajan, A., Komposch, K., Li, L., Amberg, N., Chen, L., Wculek, S.K., Hammer, M., Zenz, R., Peck-Radosavljevic, M., et al. (2014). EGFR has a tumour-promoting role in liver macrophages during hepatocellular carcinoma formation. Nat. Cell Biol. *16*, 972–977. https://doi.org/10.1038/ncb3031.
18. Liu, P.-S., Chen, Y.-T., Li, X., Hsueh, P.-C., Tzeng, S.-F., Chen, H., Shi, P.-Z., Xie, X., Parik, S., Planque, M., et al. (2023). CD40 signal rewires fatty acid and glutamine metabolism for stimulating macrophage anti-tumorigenic functions. Nat. Immunol. *24*, 452–462. https://doi.org/10.1038/s41590-023-01430-3.
19. Praktiknjo, S.D., Obermayer, B., Zhu, Q., Fang, L., Liu, H., Quinn, H., Stoeckius, M., Kocks, C., Birchmeier, W., and Rajewsky, N. (2020). Tracing tumorigenesis in a solid tumor model at single-cell resolution. Nat. Commun. *11*, 991. https://doi.org/10.1038/s41467-020-14777-0.
20. Zhang, Q., He, Y., Luo, N., Patel, S.J., Han, Y., Gao, R., Modak, M., Carotta, S., Haslinger, C., Kind, D., et al. (2019). Landscape and Dynamics of Single Immune Cells in Hepatocellular Carcinoma. Cell *179*, 829–845.e20. https://doi.org/10.1016/j.cell.2019.10.003.
21. Sun, Y., Wu, L., Zhong, Y., Zhou, K., Hou, Y., Wang, Z., Zhang, Z., Xie, J., Wang, C., Chen, D., et al. (2021). Single-cell landscape of the ecosystem in early-relapse hepatocellular carcinoma. Cell *184*, 404–421.e16. https://doi.org/10.1016/j.cell.2020.11.041.
22. Bi, Y., Chen, J., Hu, F., Liu, J., Li, M., and Zhao, L. (2019). M2 Macrophages as a Potential Target for Antiatherosclerosis Treatment. Neural Plast. *2019*, 6724903. https://doi.org/10.1155/2019/6724903.
23. Baitsch, D., Bock, H.H., Engel, T., Telgmann, R., Müller-Tidow, C., Varga, G., Bot, M., Herz, J., Robenek, H., von Eckardstein, A., and Nofer, J.R. (2011). Apolipoprotein E induces antiinflammatory phenotype in macrophages. Arterioscler. Thromb. Vasc. Biol. *31*, 1160–1168. https://doi.org/10.1161/ATVBAHA.111.222745.
24. Wen, G., Zhang, C., Chen, Q., Luong, L.A., Mustafa, A., Ye, S., and Xiao, Q. (2015). A Novel Role of Matrix Metalloproteinase-8 in Macrophage Differentiation and Polarization. J. Biol. Chem. *290*, 19158–19172. https://doi.org/10.1074/jbc.M114.634022.
25. Guo, H., Jin, D., and Chen, X. (2014). Lipocalin 2 is a regulator of macrophage polarization and NF-κB/STAT3 pathway activation. Mol. Endocrinol. *28*, 1616–1628. https://doi.org/10.1210/me.2014-1092.
26. Alonso-Herranz, L., Sahún-Español, Á., Paredes, A., Gonzalo, P., Gkontra, P., Núñez, V., Clemente, C., Cedenilla, M., Villalba-Orero, M., Inserte, J., et al. (2020). Macrophages promote endothelial-to-mesenchymal transition via MT1-MMP/TGFβ1 after myocardial infarction. Elife *9*, e57920. https://doi.org/10.7554/eLife.57920.
27. Lee, Y.J., Wang, Q., and Rio, D.C. (2018). Coordinate regulation of alternative pre-mRNA splicing events by the human RNA chaperone proteins

hnRNPA1 and DDX5. Genes Dev. *32*, 1060–1074. https://doi.org/10.1101/gad.316034.118.

28. Park, S., Mossmann, D., Chen, Q., Wang, X., Dazert, E., Colombi, M., Schmidt, A., Ryback, B., Ng, C.K.Y., Terracciano, L.M., et al. (2022). Transcription factors TEAD2 and E2A globally repress acetyl-CoA synthesis to promote tumorigenesis. Mol. Cell *82*, 4246–4261.e11. https://doi.org/10.1016/j.molcel.2022.10.027.
29. Li, F., Wu, R., Cui, X., Zha, L., Yu, L., Shi, H., and Xue, B. (2016). Histone Deacetylase 1 (HDAC1) Negatively Regulates Thermogenic Program in Brown Adipocytes via Coordinated Regulation of Histone H3 Lysine 27 (H3K27) Deacetylation and Methylation. J. Biol. Chem. *291*, 4523–4536. https://doi.org/10.1074/jbc.M115.677930.
30. Snelgrove, R.J., Jackson, P.L., Hardison, M.T., Noerager, B.D., Kinloch, A., Gaggar, A., Shastry, S., Rowe, S.M., Shim, Y.M., Hussell, T., and Blalock, J.E. (2010). A critical role for LTA4H in limiting chronic pulmonary neutrophilic inflammation. Science *330*, 90–94. https://doi.org/10.1126/science.1190594.
31. Sutendra, G., Kinnaird, A., Dromparis, P., Paulin, R., Stenson, T.H., Haromy, A., Hashimoto, K., Zhang, N., Flaim, E., and Michelakis, E.D. (2014). A nuclear pyruvate dehydrogenase complex is important for the generation of acetyl-CoA and histone acetylation. Cell *158*, 84–97. https://doi.org/10.1016/j.cell.2014.04.046.
32. Yoshinaga, K., Obata, H., Jurukovski, V., Mazzieri, R., Chen, Y., Zilberberg, L., Huso, D., Melamed, J., Prijatelj, P., Todorovic, V., et al. (2008). Perturbation of transforming growth factor (TGF)-β1 association with latent TGF-β binding protein yields inflammation and tumors. Proc. Natl. Acad. Sci. USA *105*, 18758–18763. https://doi.org/10.1073/pnas.0805411105.
33. Li, X., Ke, Y., Hernandez, A.L., Yu, J., Bian, L., Hall, S.C., Nolan, K., Wang, J.H., Young, C.D., and Wang, X.-J. (2023). Inducible nitric oxide synthase (iNOS)-activated Cxcr2 signaling in myeloid cells promotes TGFβ-dependent squamous cell carcinoma lung metastasis. Cancer Lett. *570*, 216330. https://doi.org/10.1016/j.canlet.2023.216330.
34. Zhou, J., Lyu, N., Wang, Q., Yang, M., Kimchi, E.T., Cheng, K., Joshi, T., Tukuli, A.R., Staveley-O'Carroll, K.F., and Li, G. (2023). A novel role of TGFBI in macrophage polarization and macrophage-induced pancreatic cancer growth and therapeutic resistance. Cancer Lett. *578*, 216457. https://doi.org/10.1016/j.canlet.2023.216457.
35. Alsamraae, M., Costanzo-Garvey, D., Teply, B.A., Boyle, S., Sommerville, G., Herbert, Z.T., Morrissey, C., Dafferner, A.J., Abdalla, M.Y., Fallet, R.W., et al. (2023). Androgen receptor inhibition suppresses anti-tumor neutrophil response against bone metastatic prostate cancer via regulation of TβRI expression. Cancer Lett. *579*, 216468. https://doi.org/10.1016/j.canlet.2023.216468.
36. Chen, J., Feng, W., Sun, M., Huang, W., Wang, G., Chen, X., Yin, Y., Chen, X., Zhang, B., Nie, Y., et al. (2024). TGF-β1-Induced SOX18 Elevation Promotes Hepatocellular Carcinoma Progression and Metastasis Through Transcriptionally Upregulating PD-L1 and CXCL12. Gastroenterology *167*, 264–280. https://doi.org/10.1053/j.gastro.2024.02.025.
37. Yin, C., Zhang, C., Wang, Y., Liu, G., Wang, N., Liang, N., Zhang, L., Tu, Q., Lv, J., Jiang, H., et al. (2025). ALDOB/KAT2A interactions epigenetically modulate TGF-β expression and T cell functions in hepatocellular carcinogenesis. Hepatology *81*, 77–93. https://doi.org/10.1097/HEP.0000000000000704.
38. Colak, S., and Ten Dijke, P. (2017). Targeting TGF-β Signaling in Cancer. Trends Cancer *3*, 56–71. https://doi.org/10.1016/j.trecan.2016.11.008.
39. Mariathasan, S., Turley, S.J., Nickles, D., Castiglioni, A., Yuen, K., Wang, Y., Kadel, E.E., Koeppen, H., Astarita, J.L., Cubas, R., et al. (2018). TGFβ attenuates tumour response to PD-L1 blockade by contributing to exclusion of T cells. Nature *554*, 544–548. https://doi.org/10.1038/nature25501.
40. Lan, Y., Zhang, D., Xu, C., Hance, K.W., Marelli, B., Qi, J., Yu, H., Qin, G., Sircar, A., Hernández, V.M., et al. (2018). Enhanced preclinical antitumor activity of M7824, a bifunctional fusion protein simultaneously targeting PD-L1 and TGF-β. Sci. Transl. Med. *10*, eaan5488. https://doi.org/10.1126/scitranslmed.aan5488.
41. Rikimaru, T., Taketomi, A., Yamashita, Y.i., Shirabe, K., Hamatsu, T., Shimada, M., and Maehara, Y. (2007). Clinical significance of histone deacetylase 1 expression in patients with hepatocellular carcinoma. Oncology *72*, 69–74. https://doi.org/10.1159/000111106.
42. Charni-Natan, M., and Goldstein, I. (2020). Protocol for Primary Mouse Hepatocyte Isolation. STAR Protoc. *1*, 100086. https://doi.org/10.1016/j.xpro.2020.100086.
43. Toda, G., Yamauchi, T., Kadowaki, T., and Ueki, K. (2021). Preparation and culture of bone marrow-derived macrophages from mice for functional analysis. STAR Protoc. *2*, 100246. https://doi.org/10.1016/j.xpro.2020.100246.
44. Qiu, X., Yang, S., Wang, S., Wu, J., Zheng, B., Wang, K., Shen, S., Jeong, S., Li, Z., Zhu, Y., et al. (2021). M6A Demethylase ALKBH5 Regulates PD-L1 Expression and Tumor Immunoenvironment in Intrahepatic Cholangiocarcinoma. Cancer Res. *81*, 4778–4793. https://doi.org/10.1158/0008-5472.CAN-21-0468.
45. Yang, S., Qian, L., Li, Z., Li, Y., Bai, J., Zheng, B., Chen, K., Qiu, X., Cai, G., Wang, S., et al. (2023). Integrated Multi-Omics Landscape of Liver Metastases. Gastroenterology *164*, 407–423.e17. https://doi.org/10.1053/j.gastro.2022.11.029.
46. Cong, L., and Zhang, F. (2015). Genome engineering using CRISPR-Cas9 system. Methods Mol. Biol. *1239*, 197–217. https://doi.org/10.1007/978-1-4939-1862-1_10.

STAR★METHODS

KEY RESOURCES TABLE

REAGENT or RESOURCE	SOURCE	IDENTIFIER
Antibodies		
Ly-6G/C (Gr-1); Mouse; 141Pr	Fluidigm	3141005B
CD44; Human/Mouse; 171Yb	Fluidigm	3171003B; RRID:AB_2895121
CD115; Mouse; 144ND	Fluidigm	3144012B; RRID:AB_2895116
CD4; Mouse; 145ND	Fluidigm	3145002B; RRID:AB_2687832
CD11c; Mouse; 142ND	Fluidigm	3142003B; RRID:AB_2814737
CD274 (PD-L1); Mouse; 153Eu	Fluidigm	3153016B; RRID:AB_2687837
Ly-6C; Mouse; 162Dy	Fluidigm	3162014B; RRID:AB_2922921
CD3e; Mouse; 152Sm	Fluidigm	3152004B; RRID:AB_3076460
CD19; Mouse; 166Er	Fluidigm	3166015B; RRID:AB_2687846
Ly-6G; Mouse; 151Eu	Fluidigm	3151010B
CD11b (Mac-1); Mouse; 148ND	Fluidigm	3148003B; RRID:AB_2814738
CD54 (ICAM-1); Mouse; 163Dy	Fluidigm	3163020B
CD24; Mouse; 150ND	Fluidigm	3150009B; RRID:AB_2916042
CD8a; Mouse; 168Er	Fluidigm	3168003B; RRID:AB_2811241
CD45; Mouse; 89Y	Fluidigm	3089005B; RRID:AB_2651152
CD86; Mouse; 172Yb	Fluidigm	3172016B; RRID:AB_2922923
FceR1a; Mouse; 176Yb	Fluidigm	3176006B; RRID:AB_2922925
CD206 (MMR); Mouse; 169Tm	Fluidigm	3169021B; RRID:AB_2832249
I-A/I-E; Mouse; 209Bi	Fluidigm	3209006B; RRID:AB_2885025
F4/80; Mouse; 146ND	Fluidigm	3146008B; RRID:AB_2895117
CX3CR1; Mouse; 164Dy	Fluidigm	3164023B; RRID:AB_2832247
CD40; Mouse; 161Dy	Fluidigm	3161020B; RRID:AB_2885020
CD69; Mouse; 143ND	Fluidigm	3143004B; RRID:AB_2827881
CD279 (PD-1); Mouse; 159Tb	Fluidigm	3159024B; RRID:AB_2687839
CD38; Mouse; 175Lu	Fluidigm	3175014B; RRID:AB_2895122
CD45R (B220); Human/Mouse; 160Gd	Fluidigm	3160012B
CTLA4; Mouse; 154Sm	Fluidigm	3154008B; RRID:AB_3665152
NK1.1; Mouse; 170Er	Fluidigm	3170002B; RRID:AB_2885023
Foxp3; Mouse; 158Gd	Fluidigm	3158003A; RRID:AB_2814740
Anti-Mannose Receptor	Abcam	ab252921
Anti-Mannose Receptor	Abcam	ab300621; RRID:AB_2935881
Anti-F4/80	Abcam	ab300421; RRID:AB_2936298
Anti-CD68	CST	76437S; RRID:AB_2799882
Anti-Flag	R&D Systems	MAB8529; RRID:AB_3659198
Anti-LTA4H	Abcam	ab133512; RRID:AB_2892643
Anti-JNK1+JNK2+JNK3	Abcam	ab179461; RRID:AB_2744672
Anti-phosph- JNK1+JNK2+JNK3	Abcam	ab124956; RRID:AB_10973183
Anti-*c*-jun	Abcam	ab40766; RRID:AB_731602
Anti-phosph-*c*-jun	Abcam	ab32385; RRID:AB_726900
Anti-p38	Beyotime	AM065; RRID:AB_2617174
Anti-phosph-p38	Beyotime	AM063; RRID:AB_2617173
Anti-ERK	Abcam	ab184699; RRID:AB_2802136
Anti-phosph-ERK	Abcam	ab278538; RRID:AB_3076213

(*Continued on next page*)

Continued

REAGENT or RESOURCE	SOURCE	IDENTIFIER
Anti-LTBP1	Abcam	ab78294; RRID:AB_1952060
Anti-HNRNPA1	Abcam	ab5832; RRID:AB_305145
Anti-Pan ser/thr phosphorylation	Abmart	T91067; RRID:AB_2936786
Anti-CD40	Abcam	ab252428
Anti-PD-L1	R&D Systems	MAB90781; RRID:AB_2921258
Anti-CD11c	Abcam	ab219799; RRID:AB_2864725
Anti-Ly6G/6C	Santa Cruze	sc-59338; RRID:AB_2167795
Anti-GAPDH	Beyotime	AF5009
Anti-β-Actin	CST	3700S; RRID:AB_2242334
Anti-CD8	Abcam	ab217344; RRID:AB_2890649
Anti-PD-1	Abcam	ab214421; RRID:AB_2941806
Anti-GZMB	Abcam	ab255598; RRID:AB_2860567
Anti-LTA4H	Origene	CF500665
Anti-H3K27ac	Abcam	ab4729 RRID:AB_2118291
Anti-IgG	Abcam	ab171870 RRID:AB_2687657
Anti-Histone H3	Bioss	BSM-33042M
Secondary Antibody, HRP, IHC, mouse and rabbit	Longislandab	D-3004-15
IRDye 680RD secondary rabbit antibody	LI-COR	926-68071; RRID:AB_10956166
IRDye 800CW secondary mouse antibody	LI-COR	926-32210; RRID:AB_3096013
Antibody of PD-1 blockade	BioXcell	BE0146; RRID:AB_10949053
Antibody of TGF-β blockade	BioXcell	BE0057; RRID:AB_1107757
Biological samples		
Human HCC tissue microarray including tumor and adjacent liver tissues	Eastern Hepatobiliary Surgery Hospital (Shanghai, China)	N/A
Matching fresh HCC tumor and adjacent liver tissues	Eastern Hepatobiliary Surgery Hospital (Shanghai, China)	N/A
Formalin-fixed HCC sections from patients with ICIs	Wuhan Union Hospital (Wuhan, China)	N/A
Chemicals, peptides, and recombinant proteins		
N-nitrosodiethylamine (DEN)	Sigma-Aldrich	N0756
Carbon tetrachloride (CCl4)	Sinopharm	56-23-5
Matrigel	Corning	356237
Bovine serum albumin	Sigma-Aldrich	A4737
3% hydrogen peroxide	Sinopharm	7722-84-1
Citrate Buffer	Sigma-Aldrich	C9999
WB and IP lysis buffer	Yeasen	20118ES60
Protease inhibitor cocktail	Yeasen	20124ES03
Phosphatase inhibitor cocktail	Yeasen	20109ES05
Protein A + G beads	MCE	HY-K0202
RNase A/T1	Thermo Fisher	EN0551
G418	Beyotime	ST081
TRIzol reagent	Thermo Fisher	15596026
SYBR Green	Roche	04707516001
TGFβ ELISA kit	R&D Systems	DB100C
hydrochloric acid (HCl)	Sinopharm	7647-01-0
sodium hydroxide (NaOH)	Sinopharm	1310-73-2
Liberase	Merck	05401020001
L-glutamine	Thermo Fisher	A2916801

(*Continued on next page*)

Continued

REAGENT or RESOURCE	SOURCE	IDENTIFIER
LTB4	Cayman	20110
JNK-IN-8	Aladdin	J125321
LY255283	MCE	HY-15744
U-75302	Cayman	70705
ACK lysis buffer	Thermo Fisher	A1049201
M-CSF	Novoprotein	CB34
IL-4	Novoprotein	CK74
LPS	Beyotime	S1732
IFN-γ	Novoprotein	C746
Puromycin	Beyotime	ST551
Hoechst 33342	Sigma-Aldrich	B2883
Actinomycin D	Sigma-Aldrich	A9415
Critical commercial assays		
Opal Polaris 7 Color Manual IHC detection kit	Akoya	NEL86100KT
DAB peroxidase substrate kit	Beyotime	P0203
TUNEL apoptosis kit	Beyotime	C1098
Reverse transcription kit	Yeasen	11149ES
ALT activity assay kits	Nanjing Jiancheng	C009-2-1
AST activity assay kits	Nanjing Jiancheng	C010-2-1
VAHTS Total RNA-seq (H/M/R) Library Prep Kit for Illumina	Vazyme	NR603
Nuclear and cytoplasmic extract kit	Yeasen	20126ES
RIP RNA-Binding Protein Immunoprecipitation Kit	FITGENE	FI8707
Chromatin Extraction Kit	Abcam	ab117152
CHIP Kit Magnetic- One Step	Abcam	ab156907
PCR purification Kit	Beyotime	D0033
NEBNext® Ultra™ DNA Library Prep Kit for Illumina	NEB	E7645L
jetPRIME *in vitro* DNA & siRNA transfection reagent kit	Polyplus	101000027
Deposited data		
Raw transcriptome sequencing data	This paper	NGDC: CRA022579
Raw data of mass cytometry	This paper	FlowRepository: FR-FCM-Z7W7
Raw LC-MS/MS data	This paper	ProteomeXchange: PXD060326
Raw CHIP sequencing data	This paper	NGDC: CRA021482
CHCC-HBV proteomic cohort	Gao Qiang et al.[13]	NODE database: OEP000321
Experimental models: Cell lines		
Hepa1-6 cell line	ATCC	CRL-1830, RRID: CVCL_0327
HepG2 cell line	ATCC	HB-8065, RRID:CVCL_0027
Experimental models: Organisms/strains		
C57 L/J mouse	Jackson Laboratory	RRID:IMSR_JAX:000668
$LTA4H^{flox/flox}$ transgenic mouse	GemPharmatech	N/A
Alb-cre transgenic mouse	GemPharmatech	T064038
CAG-cre transgenic mouse	GemPharmatech	RRID:IMSR_GPT:T050269
$BLT1^{KO}$ mouse	A gift from Prof. Rui He's lab in the Fudan University Shanghai Medical College	RRID:IMSR_JAX:00810
Oligonucleotides		
qRT-PCR Primer sequence	This paper	See Table S8

(*Continued on next page*)

Continued

REAGENT or RESOURCE	SOURCE	IDENTIFIER
Genotyping Primer sequence	This paper	See Table S8
shControl	This paper	TTCTCCGAACGTGTCACGT
sh*Hnrnap1*-3	This paper	GGAUGGAAGAGUUGUGGAATT
sh*Ltbp1*-1	This paper	CCCAAGAAACAATCCTATCAT
sh*Ltbp1*-2	This paper	CCCAACATAGTCAATATCCAT
sh*Ltbp1*-3	This paper	CCCTCCAAATTTCACAGGAAA
sgRNA targeting mouse *Lta4h*	This paper	See STAR Methods
siRNA targeting mouse *Hnrnpa1*	This paper	See STAR Methods
siRNA targeting mouse *Hdac1*	This paper	See STAR Methods
siRNA targeting mouse *Hdac2*	This paper	See STAR Methods
Recombinant DNA		
Plasmids pGC-FU-3FLAG-CBh-gcGFP-IRES-puromycin	Genechem	GV492
Plasmids LV-sgRNA-firefly_Luciferase-IRES-neo	Genechem	GV807
Plasmids Ubi-3FLAG-Cas9-SV40-puromycin	Genechem	GV396
Plasmids hU6-MCS-Ubiquitin-EGFP-IRES-puromycin	Genechem	GV248
Software and algorithms		
Cytobank	Beckman Coulter	https://premium.cytobank.org/cytobank; RRID:SCR_014043
Cytofkit	N/A	https://github.com/JinmiaoChenLab/cytofkit
FastQC v0.11.5	N/A	https://github.com/s-andrews/FastQC; RRID:SCR_014583
STAR version 2.5.3a	N/A	https://github.com/alexdobin/STAR; RRID:SCR_005622
DESeq2 v1.16.1	N/A	https://github.com/thelovelab/DESeq2; RRID:SCR_015687
ClusterProfiler	N/A	https://doi.org/10.1089/omi.2011.0118; RRID:SCR_016884
R version 4.2.0	R Core Team 2017	https://www.r-project.org; RRID:SCR_001905
RStudio	Posit.co	https://posit.co/download/rstudio-desktop/; RRID:SCR_000432
ggplot2 (v3.5.5)	N/A	https://ggplot2-book.org/; RRID:SCR_014601
Bowtie2 (v2.4.2)	N/A	https://github.com/BenLangmead/bowtie2;
GraphPad Prism	GraphPad Software	http://www.graphpad.com/; RRID:SCR_002798

EXPERIMENTAL MODEL AND STUDY PARTICIPANT DETAILS

Tissue microarray and patients

The HCC tissue microarray cohort (TMA HCC cohort), which included 133 pairs of HCC tumor tissues and matched adjacent liver tissues (118 males and 15 females; age range, 45–75 years), was collected from Eastern Hepatobiliary Surgery Hospital (Shanghai, China) between January 2010 and February 2017. Follow-up data were summarized at Match 2018. The primary endpoints of the study were time to recurrence and overall survival. The time to recurrence was defined as the duration from the date of resection to the date of diagnosis of tumor recurrence. Overall survival was calculated from the date of resection to the date of death or the last follow-up. HCC TMA chips were used for IHC staining of LTA4H. In addition, clinical HCC samples included 10 pairs of fresh HCC tissues and adjacent liver tissues (10 males; age range, 48–73 years), which were

collected after surgical resection and were subjected to western blot (WB) analysis, real-time quantitative PCR and ELISA assay. 13 formalin-fixed HCC sections from patients with ICIs (10 males and three females; age range, 32–72 years) were collected from Wuhan Union Hospital and were subjected to multiplex immunohistochemistry. All samples were randomly collected. To ensure a balanced distribution between the responder (n = 6) and non-responder (n = 7) groups in the ICI-treated patients, the randomization was stratified by response status.

All patient samples were obtained with the approval of the hospital's Research Ethics Committee, and written informed consent was provided by all participants.

Mice and HCC mouse model

The animal experiments were performed following institutional guidelines and approved by the Ethics Committee of Fudan University. The mice used in this study (LTA4H$^{flox/flox}$, *Alb*-Cre, CAG-Cre, and C57BL/6 mice) were obtained from GemPharmatech and maintained in specific pathogen-free housing. C57L/J mice were acquired from the Jackson Laboratory. BLT1 knockout (BLT1^{KO}) mice were a gift from Prof. Rui He's lab in the Fudan University Shanghai Medical College, Fudan University, China. LTA4H^{KO} mice were obtained via the breeding of LTA4H$^{flox/flox}$ and Cag-Cre transgenic mice. We also generated mice with liver-specific KO (ΔHEP) of LTA4H by crossing *Alb*-Cre transgenic mice with homozygous floxed LTA4H mice. The primers used for genotyping can be found in Table S8.

LTA4H$^{\Delta hep}$ and littermate LTA4H$^{f/f}$ male mice and LTA4H^{KO} male mice were injected i.p. with a single dose of N-nitrosodiethylamine (DEN, 25 mg/kg) on postnatal day 14 to induce HCC model. For the DEN combined with CCL_4-induced HCC model, the above male mice were also administered with DEN (i.p. injection of 25 mg/kg at 14 days of age), followed by CCL_4 treatment (starting at 6 weeks of age; 2 mL/kg, 25% dissolved in olive oil, once per week via i.p. injection) for 22 continuous weeks.

Male C57L/J mice aged 6–8 weeks were used for orthotopic implantation. 2×10^6 Hepa1-6 cells that were transfected with the indicated lentivirus were resuspended in 50ul of a mixture of PBS and Matrigel mixture (1:1) and then injected into the left lobe of the liver under isoflurane anesthesia. For macrophages depletion, mice were injected intraperitoneally with clodronate-containing liposomes or control liposomes (200μL of suspension/10g of mouse weight) 5 days before orthotopic implantation, and on day 1, day 5 and day 10 during experiment. For drug intervention, 5 days after model construction, mice with scramble and LTA4H KO tumors were randomly divided into 4 groups (5 mice per group). After the first bioluminescent imaging, mice were injected intraperitoneally with 100 μg of anti-PD-1 antibody (BioXcell, BE0146), 100μg of anti-TGF-β antibody (BioXcell, BE0057) or combination or IgG control every three days for a total of three injections. The live imaging experiments were performed three times during this experiment. Liver samples were harvested at the experimental endpoint (day 14).

Isolation and treatment of primary hepatocytes

Primary mouse hepatocytes were isolated by Liberase perfusion.[42] Livers from LTA4H$^{f/f}$ and LTA4H^{KO} male mice aged 6–8 weeks were first perfused with HBSS supplemented with 25 mM HEPES and 0.5 mM EDTA, followed by Liberase digestion (Merck, 05401020001). Isolated hepatocytes were washed with low glucose DMEM and collected by centrifugation at 50 × g. A total of 4×10^5 cells were plated on 6-well plates in low-glucose DMEM containing 10% fetal calf serum and a combination of penicillin and streptomycin. The maintenance medium (Williams E medium supplemented with 2 mM glutamine and a combination of penicillin and streptomycin) was changed after 4 h. The cells were cultured in a 5% CO_2 cell culture incubator at 37 °C. The next day, the cells were treated with DEN (25 ng/mL), LTB4 (100 nM, Cayman, 20110) and inhibitors including JNK-IN-8 (2.5 μM, Aladdin, J125321), LY255283 (5 μM, MCE, HY-15744) and U-75302 (200 nM, Cayman, 70705), as indicated in the figures. Cells were harvested at the indicated time points, and protein and RNA were isolated.

Isolation of bone marrow-derived macrophages (BMDMs) and coculture with conditioned medium

BMDMs were prepared by methods described previously.[43] Briefly, bone marrow cells were obtained by flushing the femurs and tibias of 6 to 8-week-old wild-type C57BL/6 male mice or LTA4H$^{f/f}$ and LTA4H^{KO} male mice. Red blood cells were lysed with ACK lysis buffer (Thermo Fisher Scientific, A1049201). Then, the cells were cultured in BMDM culture medium (complete 1640 medium supplemented with macrophage colony stimulating factor [M-CSF, 10 ng/mL, Novoprotein, CB34]). On day 6, the nonadherent cells were removed and fresh BMDM culture medium was added. On day 7, M2 macrophages were stimulated with IL-4 (10 ng/mL, Novoprotein, CK74) for 2 days, and M1 macrophages were stimulated with LPS (10 ng/mL, Beyotime, S1732) and IFN-γ (5 ng/mL, Novoprotein, C746) for 2 days. The cells were cultured in a 5% CO_2 cell culture incubator at 37 °C.

For coculture with Hepa1-6 conditioned medium, the culture medium of Hepa1-6 cells was treated with hydrochloric acid (HCl) to activate latent TGF-β, and then HCL was neutralized with sodium hydroxide (NaOH) to obtain the available conditioned medium. Then, the medium of the BMDMs was changed to conditioned medium on day 6. IL-4 or LPS and IFN-γ and anti-TGF-β were used on day 7. Following qPCR or immunofluorescence experiments were performed after 2 days.

Cell lines culture and treatment

Hepa1-6 and HepG2 cell lines were cultured in DMEM supplemented with 10% FBS and a combination of penicillin and streptomycin. The cell lines were authenticated by STR profiling and regularly tested for mycoplasma infection. The mouse LTA4H coding

sequence were cloned into the GV492 plasmid, and the synthesized plasmids were then transfected into 293T cells for LTA4H lentivirus production. Hepa1-6 cells stably overexpressing LTA4H were generated with LTA4H lentivirus, selected with puromycin (1 mg/mL, ST551) and confirmed by western blotting. The shRNAs targeting mouse *Hnrnpa1* and *Ltbp1* were cloned into the GV116 plasmid (Target sequences seen in Key Resources Table), and the synthesized plasmids were then transfected into 293T cells for lentivirus production. Lentiviruses with each shRNA were transduced into Hepa1-6 scramble and LTA4H KO cells, which were selected with Hygromycin B (GeneChem, REVG1009). The cells were treated with LTB4 (100 nM, Cayman, 20110) and inhibitors including LY255283 (5 μM, MCE, HY-15744) and U-75302 (200 nM, Cayman, 70705), as indicated in the figures. The cells were cultured in a 5% CO_2 cell culture incubator at 37 °C.

METHOD DETAILS

Mass cytometry and analyses

Single-cell suspensions from mouse liver tumors were prepared as previously described.[44] The cells were immunostained with specific antibodies against surface markers to identify various cell types listed in Key Resources Table. Antibodies were purchased from Fluidigm. Barcoding and staining were then performed according to Fluidigm's instructions as described below. Briefly, the collected cells were washed with MaxPar PBS Buffer and stained with 0.5 μM cisplatin (Fluidigm, 201064) for 2 min at room temperature. Fix I buffer (Fluidigm, 201065) was used to fix the cells at room temperature for 10 min, followed by washing the fixed cells with Barcode Perm buffer (Fluidigm, 201067) and centrifugation at 800 × g for 5 min to pellet the cells. A Cell-ID 20-Plex Pd Barcoding Kit (Fluidigm, 201060) was used to barcode the above fixed cells, as directed by the manufacturer. Ten barcoded samples were pooled for antibody cocktail staining for 30 min at room temperature. After staining, the cells were incubated in Cell-ID Intercalator-Ir (Fluidigm, 201192A) solution overnight at 4°C. The samples were then washed twice with ddH_2O, and filtered into 30 μm strained cap tubes and diluted in ddH_2O containing 10% EQ Four Element Calibration Beads (Fluidigm, 201078). CyTOF data were acquired and analyzed as previously described.[45] The Helios instrument was checked and calibrated prior to each analysis as per the manufacturer's guidelines. Following Fluidigm's recommendation, FCS files were randomized and normalized using EQ beads signal. After that, the files were concatenated, debarcoded, and randomized as instructed by Fluidigm. The gating of live lymphocytes was carried out in Cytobank. Clustering analysis was done with t-distributed stochastic neighbor embedding (t-SNE) and PhenoGraph algorithms in R package Cytofkit with default settings (seed = 42, t-SNE perplexity = 30, t-SNE max iterations = 1000, nearest neighbors K = 30, Euclidean distance). Diffusion maps were generated from Cytofkit ShinyApp interactive interface. The other visualizations were displayed by R package. For the definition of major cell populations, briefly, CD45 was used to define lymphocytes, CD3e for T cells, CD45R and CD19 for B cells, GR-1 and LY-6G for neutrophils, I-A/I-E and CD11c for dendritic cells, NK1.1 for NK cells, and F4/80 along with CD11b for macrophages.

H&E and immunohistochemistry

H&E and immunohistochemistry (IHC) were performed as previously described.[45] Briefly, H&E and IHC were performed using 4-μm-thick formalin-fixed paraffin-embedded sections. After baking at 60°C for an hour, the tissue sections were deparaffinized with xylene and rehydrated with graded ethanol. For H&E staining, hematoxylin and eosin staining was performed after deparaffinization. For IHC staining, inactivation of endogenous peroxidases was carried out using 3% hydrogen peroxide for 20 min, followed by washing with double-distilled water (ddH_2O). Antigen retrieval was performed using 0.01 mol/L citrate buffer solution (pH 6.0) in a pressure cooker. Blocking was performed with 1% bovine serum albumin (BSA) solution at 37°C for 30 min. Then the sections were incubated with primary antibodies at 4°C for overnight, followed by incubation with secondary peroxidase-conjugated antibodies for 30 min at room temperature. Staining was visualized with a DAB peroxidase substrate kit (Beyotime, P0203). Then, the H&E and IHC stained sections were dehydrated and covered with a coverslip. TUNEL staining was carried out utilizing a TUNEL apoptosis kit (Beyotime, C1098) following the manufacturer's specifications. Images were obtained with a Leica Aperio AT2 instrument.

LTA4H (antibody: Abcam, ab133512) staining of the TMA was scored according to intensity (0–3) and positive rate (1–4). Briefly, staining intensity was categorized by a pathologist in a double-blind manner as follows: no staining (0), weak staining (1), moderate staining (2), and strong staining (3). The positive rate of staining was assessed by the percentage of positive cells, with scores assigned as follows: ≤25% (1), 26–50% (2), 51–75% (3), and 76–100% (4). The overall score was calculated by multiplying the intensity score by the positive rate score, resulting in a combined IHC score. For quantification of PCNA (antibody: A12427, Abclonal) or TUNEL-positive cells, three fields were counted per mouse to ensure a representative assessment of the staining. $TUNEL^+$ and $PCNA^+$ cells were counted using the positive cell detection function in QuPath. The parameters were set to a minimum nuclear area of 60 px^2 and a minimum circularity of 0.8 to exclude stromal and immune cells. Default parameters were used for other settings. The positive staining score was then calculated as the percentage of positive cells relative to the total (positive + negative) cells in each field. The primary antibodies used can be found in Key Resources Table.

Co-IP and LC-MS/MS proteomic assays

Cells were lysed with WB and IP lysis buffer (Yeasen, 20118ES60) supplemented with protease inhibitor cocktail (Yeasen, 20124ES03) and phosphatase inhibitor cocktail (Yeasen, 20109ES05). The lysates were incubated on ice for 30 min with occasional

mixing. The lysates were cleared by centrifugation at 12,000 rpm for 20 min at 4°C. The supernatants were incubated with an FLAG tag antibody (R&D Systems, MAB8529), LTA4H antibody (Origene, CF500665) or an HNRNPA1 antibody (Abcam, ab5832) overnight. The Protein A + G beads (MCE, HY-K0202) were added to precipitate the target protein complex with the appropriate antibody. Then, the immunoprecipitants were washed five times with lysis buffer. Finally, the bound proteins were eluted at 95°C for 5 min in 40μL of 1×SDS-PAGE sample loading buffer. For RNase treatment, the samples were treated with 1:1000 RNase A/T1 (Thermo Fisher Scientific, EN0551) for 15 min at 37°C. After co-IP, the samples were subjected to LC-MS or western blotting using the following antibodies: LTA4H antibody (Abcam, ab133512), HNRNPA1 antibody (Abcam, ab5832) and pan-ser/thr phosphorylation antibody (Abmart, T91067). LC-MS/MS analysis was performed with the support of Jingjie PTM Biolabs (Hangzhou, China) Co., Ltd.

Western blot

The lysates were fractionated by SDS-PAGE and transferred to nitrocellulose membranes. Nonspecific binding sites were blocked with 5% BSA in TBST solution for 1 h at room temperature. The NC membranes were incubated with specific antibodies overnight at 4°C followed by washing with TBST three times. Several wash steps after 1 h incubation with secondary rabbit antibody (IRDye 680RD, LI-COR, 926–68071) and mouse antibody (IRDye 800CW, LI-COR, 926–32210) were executed. Odyssey scanner was used for visualization. Quantification of protein expression levels was performed using β-actin protein level as a reference using the ImageJ software. Quantification of JNK and c-jun phosphorylation levels was performed using total JNK/c-jun protein level as a reference. Quantification of co-immunoprecipitated protein was performed using immunoprecipitated protein level as a reference. The primary antibodies used can be found in Key Resources Table.

Generation of LTA4H KO Hepa1-6 cell lines using CRISPR/Cas9

The sgRNAs were designed with a web tool, as described previously.[46] The Cas9 coding sequence were cloned into the GV396 plasmid, and the synthesized plasmids were then transfected into 293T cells for lentivirus production. Cas9-expressing Hepa1-6 cells were generated using Cas9 lentivirus and selected with puromycin. The sgRNAs were modified manually to add *BbsI* restriction sites. The sgRNAs targeting mouse *Lta4h* were cloned into the GV807 plasmid, and the synthesized plasmids were then transfected into 293T cells for lentivirus production. Lentiviruses with each sgRNA were transduced into Cas9-expressing Hepa1-6 cells. The cells were then selected with G418 (Beyotime, ST081) for 2 days, divided and placed in 96-well plates; 10 days later, single clones were picked up. The effect of the knockout was determined by immunoblotting. The following control sgRNA and sgRNA targeting *Lta4h* were used: control sgRNA (5′-CGCTTCCGCGGCCCGTTCAA-3′), sgRNA-1 (5′-CTCATGAGTGCCATCCGTGA-3′), sgRNA-2 (5′-CTCACTCCTGAACAGACGTC-3′) and sgRNA-3 (5′-AGGTTACAAAGGGTCACCGA-3′).

Multiplex immunohistochemistry (mIHC)

The mIHC assay was performed as previously reported.[45] Mouse liver tumor sections were stained with Opal520 dye (CD206), Opal570 dye (F4/80), Opal620 dye (CD11c), Opal690 dye (PD-L1) and DAPI with an Opal 6-Plex Manual Detection Kit (Akoya Biosciences, NEL811001KT) and scanned using a Vectra 3.0 Pathology Imaging System Microscope. The clinical HCC samples were stained with Opal520 dye (LTA4H), Opal570 dye (CD206), Opal690 dye (CD68) and DAPI. Information of the antibodies used in this section can be found in Key Resources Table. After serial dewaxing and rehydration, the slides were fixed with 10% neutral buffered formaldehyde for 20 min. Heat-induced antigen retrieval was performed using citrate antigen retrieval solution in a microwave oven for 30 min. The slides were washed once with double-distilled water and TBST, blocked with blocking buffer, and stained with antibodies according to the manufacturer's manual. DAPI was used as a nuclear counterstain. The digital images were then analyzed with QuPath. For quantification of mIHC data, we employed a double-blind method using QuPath to select three equal-sized regions from each sample. We then performed cell segmentation using cell detection function in QuPath. For quantification of LTA4H intensity in tumor cells, the analysis was restricted to cells with a nuclear area >30 μm^2 and nuclear circularity >0.8 and CD68 intensity <20. The thresholds were determined based on the average values of parameters (nuclear area, nuclear circularity and CD68 intensity) obtained from 50 randomly selected, clearly identifiable tumor cells. The LTA4H expression data from the tumor cells were averaged to determine the LTA4H expression level in tumor cells for each mouse. To quantify $CD206^+$ macrophages, $CD40^+$ macrophages, $CD8^+$ T cells, $PD\text{-}1^+CD8^+$ T cells, $GZMB^+CD8^+$ T cells, thresholds for each marker were set based on the average values derived from clearly identifiable cell populations. Cells with marker expression exceeding the threshold were defined as positive.

Quantitative real-time PCR (qPCR)

Total RNA was extracted from cells and tissues using TRIzol reagent (Thermo Fisher Scientific, 15596026) according to the manufacturer's recommendation. The extracted RNA was used to synthesize complementary DNA using a reverse transcription kit (Yeasen, 11149ES). Quantitative real-time PCR was performed using SYBR Green (Roche, 04707516001) and LightCycler 480 real-time PCR systems following the manufacturer's protocol. The expression of the indicated genes was normalized to that of *Actb* by $2^{-\Delta\Delta Ct}$. The RNA immunoprecipitated by HNRNPA1 antibody was normalized to the input fraction. Chromatin-immunoprecipitated DNA using H3K27ac antibody was normalized by dividing the amount of the corresponding target in the input fraction. The primers used are shown in Table S8.

ELISA of total TGF-β and active TGF-β

The levels of total TGF-β and active TGF-β were determined using a mouse TGF-β ELISA kit (R&D Systems, DB100C) according to the manufacturer's instructions. For total TGF-β detection, hydrochloric acid (HCl) was used to activate the latent TGF-β in the cell culture supernatant and mouse serum, and then HCL was neutralized with sodium hydroxide (NaOH) to obtain the available samples. For active TGF-β detection, no acid treatment of the sample was needed. Notably, the cell culture medium used for TGF-β detection should be replaced with medium without serum. The absorbance was measured with a spectrophotometer at 450 nm.

AST and ALT assays

AST and ALT levels in serum from DEN-induced mouse HCC model after sacrifice, which are generally associated with hepatic damage, were assayed using ALT (Nanjing Jiancheng, C009-2-1) and AST (Nanjing Jiancheng, C010-2-1) activity assay kits according to the manufacturer's instructions with appropriate calibration controls. The absorbance at 510 nm was obtained with a Tecan multifunctional microplate reader.

RNA sequencing and analysis

RNA-seq library preparation was carried out using the VAHTS Total RNA-seq (H/M/R) Library Prep Kit for Illumina (Vazyme, NR603), followed by sequencing on a Nova6000 sequencer (Illumina, USA) with the PE150 strategy. Raw FASTQ files were processed using FastQC v0.11.5. RNA sequencing reads were mapped to the GRCm38 mouse genome assembly using STAR version 2.5.3a with Ensembl annotations. DESeq2 v1.16.1 was used for sample normalization and differential expression analysis. Differentially expressed genes were subjected to Kyoto Encyclopedia of Genes and Genomes (KEGG) enrichment analysis with the ClusterProfiler R package.

Nucleocytoplasmic separation

Nucleocytoplasmic separation was carried out with a nuclear and cytoplasmic extract kit (Yeasen, 20126ES). Following the methods described in this kit, Hepa1-6 cells subjected to different treatments were harvested for extraction of the cytoplasmic and nuclear proteins. LTA4H was detected by western blot analysis, and histone H3 and GAPDH were used as the internal controls.

Immunofluorescence

For immunofluorescence, hepatocytes or Hepa1-6 cells were seeded into 12-well plates with cell climbing slices at a density of 3×10^5 cells/well. BMDMs were seeded into 24-well plates at a density of 8×10^5 cells/well. The cells were fixed with 4% paraformaldehyde (PFA), permeated with 0.5% Triton-100 for 30 min and blocked with 5% BSA for 1 h. Primary antibodies were diluted in blocking solution and incubated with the cells at 4°C overnight. Then, the wells were washed three times with PBS and incubated with the appropriate secondary antibody for 1 h at room temperature. Finally, the cell nuclei were stained with Hoechst 33342 (Sigma-Aldrich, B2883). All operations, starting with incubation with secondary antibodies, were performed in the dark. Images of hepatocytes were acquired using a single-photon epifluorescence microscope. Images of BMDMs were acquired using an inverted fluorescence microscope. The antibodies used for immunofluorescence were against LTA4H (Abcam, ab133512, 1:100) and CD206 (Abcam, 1:200).

RNA immunoprecipitation (RIP)

RIP experiments were performed using the RIP RNA-Binding Protein Immunoprecipitation Kit (FITGENE, FI8707). Approximately 1×10^7 cells were then subjected to an equal pellet volume and resuspended in 100 μL of RIP Lysis Buffer combined with protease inhibitors cocktail and RNase inhibitors. The cell lysates were incubated with 2 μg of an antibody against HNRNPA1 (Abcam, ab5832) or IgG and rotated at 4°C overnight. After treatment with proteinase K buffer, the immunoprecipitated RNA was extracted with TRIzol reagent. The expression levels of *Ltbp1* were determined by RT-qPCR.

RNA stability assay

The RNA stability assay was performed as previously described.[44] Briefly, cells were treated with 5 μg/mL actinomycin D (Sigma-Aldrich, A9415) to inhibit global mRNA transcription. Samples were collected at the indicated time points. Total RNA was extracted for reverse transcription, and the levels of genes of interest were analyzed by qPCR.

Transient knockdown using siRNA

Hepa1-6 cells were seeded in 6-well plates. Cells were transfected with siRNA pools (10 μM) and jetPRIME *in vitro* DNA & siRNA transfection reagent kit (Polyplus, 101000027) according to the manufacturer's instructions. The cells were replenished with fresh complete media the next day and harvested 48 h later for RNA and Western blot analyses. The sequences used for siRNAs targeting *Hnrnpa1* were si*Hnrnpa1*-1 (5′-UGACAGAGGCAGUGGGAAATT-3′), si*Hnrnpa1*-2 (5′-UGGGAAGAUUGAAGUGAUATT-3′) and si*Hnrnpa1*-3 (5′- GGAUGGAAGAGUUGUGGAATT-3′). For siRNAs targeting *Hdac1*, the sequences used were as follows: si*Hdac1*-1 (5′-GAAAGAUCCUGAAGAGAAATT-3′), si*Hdac1*-2 (5′-GCAAGCAGAUGCAGAGAUUTT-3′) and si*Hdac1*-3 (5′-CCAAAGUAAUGGAGAUGUUTT-3′). For siRNAs targeting *Hdac2*, the sequences were si*Hdac2*-1 (5′-GGACAAUAGUGGUGAGAAATT-3′), si*Hdac2*-2 (5′-UGUCAAAGGUCAUGCUAAATT-3′) and si*Hdac2*-3 (5′-GCAAGAAGAAAGUGUGCUATT-3′). The sequence of negative control siRNA was 5′-UUCUCCGAACGUGUCACGUTT-3'.

Chromatin immunoprecipitation

Chromatin was isolated from hepa1-6 or HepG2 cells using Chromatin Extraction Kit (Abcam, ab117152) according to the manufacturer's instructions. CHIP assays were performed using CHIP Kit Magnetic- One Step (Abcam, ab156907) following the Abcam ChIP protocol. Immunoprecipitations were performed with H3K27ac antibody (2μg, Abcam, ab4729) or Rabbit IgG (2μg, Abcam, ab171870) and Protein A/G Magnetic beads (MCE, HY-K0202). Input DNA and immunoprecipitated DNA samples were purified by PCR purification Kit (Beyotime, D0033). Eluted DNA samples were used for either ChIP-qPCR or ChIP-seq.

CHIP-seq analysis

Sequencing libraries for immunoprecipitated chromatin DNA were prepared using the NEBNext Ultra DNA Library Prep Kit for Illumina (NEB, USA; Cat. E7645L). End-repair reactions were performed with End Repair Reaction Buffer (10X) and End Prep Enzyme Mix under the following conditions: 20°C for 30 min followed by 65°C for 30 min. NEBNext Adaptor and Blunt/TA Ligase Master Mix were used for adaptor ligation at 20°C for 15 min, followed by USER Enzyme treatment at 37°C for 5 min to remove uracil bases from the adaptor. After bead purification, libraries were amplified via PCR (initial denaturation at 98°C for 10 s, followed by cycles of 98°C for 10 s, 65°C for 30 s, and 72°C for 30 s). Library size selection and purification were performed with AMPure XP Beads, and libraries were quantified with Qubit and assessed for insert size using a High-Sensitivity DNA Chip. Sequencing was carried out on an Illumina NovaSeq 6000 platform to produce 150 bp paired-end reads. Raw reads in FASTQ format were processed using fastp (v0.20.1) to remove adapter sequences, poly-N reads, and low-quality reads, resulting in clean reads for downstream analysis. These clean reads were aligned to the reference genome using Bowtie2 (v2.4.2), and peaks were called using MACS2 (v2.2.7.1). Visualizations of the called peaks were generated using IGV software.

QUANTIFICATION AND STATISTICAL ANALYSIS

GraphPad Prism and R software were used for all statistical analyses in this study. Statistical details of experiments and analyses can be found in the figure legends. The statistical tests were performed as two-sided. Results of cell culture experiments were collected from at least 3 independent biological replicates. In the animal experiments, n represents number of animals. The differences within two groups were compared by unpaired Student's t test, paired Student's t test or nonparametric Wilcoxon rank-sum test as indicated. For comparisons of multiple groups, one-way ANOVA with Tukey's multiple comparison analysis was performed. The Pearson correlation test was used to examine the significant correlation between quantitative variables. Kaplan-Meier curves (log rank test) were used for survival analysis. Bar plots represent mean ± SD. The line and box of boxplot represent median and upper and lower quartiles, respectively. For the differential gene expression analysis in GEPIA website, the *p*-values were calculated using the linear model and empirical Bayes method in the R package limma, with adjustments using the Benjamini and Hochberg method. An asterisk (*) indicates that the *p*-value is less than 0.05. *p* value less than 0.05 ($p < 0.05$) was accepted as significant.